

## RESEARCH ARTICLE

10.1002/2017JB014348

## Key Points:

- Deep seismic data over Parnaíba Basin reveals midcrustal reflectivity and a Moho that is deeper than beneath flanking regions
- Gravity modeling suggests the top of the midcrustal reflectivity marks the top of a dense body, probably of magmatic origin
- The magmatic body acts as a dense load in the lower crust, which causes a time-dependent surface flexure into which sediments accumulate

## Supporting Information:

- Supporting Information S1
- Figure S1
- Figure S2
- Figure S3
- Figure S4
- Figure S5
- Figure S6
- Figure S7
- Figure S8
- Figure S9
- Figure S10
- Figure S11
- Figure S12
- Figure S13
- Text S1
- Text S2
- Text S3

## Correspondence to:

B. Tozer,  
brookt@earth.ox.ac.uk

## Citation:

Tozer, B., A. B. Watts, and M. C. Daly (2017), Crustal structure, gravity anomalies, and subsidence history of the Parnaíba cratonic basin, Northeast Brazil, *J. Geophys. Res. Solid Earth*, 122, 5591–5621, doi:10.1002/2017JB014348.

Received 20 APR 2017

Accepted 4 JUN 2017

Accepted article online 11 JUN 2017

Published online 11 JUL 2017

## Crustal structure, gravity anomalies, and subsidence history of the Parnaíba cratonic basin, Northeast Brazil

B. Tozer<sup>1</sup> , A. B. Watts<sup>1</sup> , and M. C. Daly<sup>1</sup> 
<sup>1</sup>Department of Earth Sciences, University of Oxford, Oxford, UK

**Abstract** Cratonic basins cover more than 10% of Earth's continental surface area, yet their origin remains enigmatic. Here we use a 1400 km long, deep (20 s two-way travel time) seismic reflection profile, five wide-angle split-spread receiver gathers, gravity anomaly, and well data to constrain the origin of the Parnaíba Basin, a cratonic basin in Northeast Brazil. In the center of the basin, the depth to pre-Paleozoic basement is ~3.3 km, a zone of midcrustal reflectivity (MCR) can be traced laterally for ~250 km at depths between 17 and 25 km and Moho depth is  $42 \pm 2$  km. Gravity and  $P$  wave modeling suggests that the MCR represents the upper surface of a high density ( $2985 \text{ kg m}^{-3}$ ) and  $V_p$  ( $6.75\text{--}7.0 \text{ km s}^{-1}$ ) lower crustal body, likely of magmatic origin. Backstripping of well data shows a concave up decreasing tectonic subsidence, similar in form to that observed in rift-type basins. We show, however, that our seismic and gravity data are inconsistent with an extensional origin. Other basin forming mechanisms are therefore required. We show that an intrusive body in the lower crust that has loaded and flexed the surface of the crust, combined with sediment loading, provides a satisfactory fit to the observed gravity anomaly. A buried load model is consistent with seismic data, which suggest that the Moho is as deep or deeper beneath the basin center than its flanks and accounts for at least part of the tectonic subsidence through a viscoelastic stress relaxation that occurs in the lithosphere following load emplacement.

## 1. Introduction

Cratonic basins have typical extents on the order of a few hundred thousand to a few million square kilometers. Numbering >20 worldwide, these basins are infilled by about 3–6 km of mostly estuarine and lacustrine, marginal and shallow marine, shales, limestones, and aeolian sandstones showing offlap at their edges, younging toward their center and simple bowl-shaped geometries with minimal internal deformation [e.g., Sloss, 1963; Sleep, 1971; Sloss, 1988; Sleep et al., 1980; Xie and Heller, 2009]. Sediment accumulation rates are slow in comparison to rift-, foreland-, and strike-slip-type basins (of the order of meters to tens of meters per million years) and their tectonic subsidence spans extended periods of geological time, often on the order of several hundreds of million years [e.g., Sloss, 1963; Sleep, 1971; Sloss, 1988; Sleep et al., 1980; Armitage and Allen, 2010; Allen and Armitage, 2011].

Recent heat flow and seismic tomographic studies [e.g., Koptev and Ershov, 2011; Priestley and McKenzie, 2013] reveal that most cratonic basins are located above regions of thick (thermally defined) lithosphere. Although a few basins, such as Murzuq and Ghadames in North Africa, appear to have formed above young, thin, lithosphere [Holt et al., 2015], plate reconstructions [Cannon et al., 2014] show that most are located on old, thick lithosphere far from plate boundaries.

Hartley and Allen [1994], Klein [1995], and Allen and Armitage [2011] have reviewed the processes that have been proposed to explain cratonic basin formation. Most studies have focused on developing geodynamical models in order to explain their tectonic subsidence and the main processes can be summarized as follows: (1) thermal subsidence following lithosphere extension, thinning, and cooling; lithospheric accretion and cooling above a subduction mantle wedge; or erosion, thinning and cooling following crust and lithosphere thickening [e.g., Sleep, 1976; Sleep et al., 1980; Ahern and Mrkvicka, 1984; Nunn and Sleep, 1984; Sleep, 2009; Kadima Kabongo et al., 2011; Holt et al., 2010, 2015; Lucazeau et al., 2015; McKenzie and Priestley, 2016]; (2) lithospheric folding caused by far-field in-plane stresses [e.g., Lambeck, 1983a, 1983b; DeRito et al., 1983; Cloetingh, 1988]; (3) dense loads produced by metamorphic phase changes or cooling of igneous intrusions within the lower crust and/or mantle lithosphere [e.g., Haxby et al., 1976; Nunn and Aires, 1988; Fowler and Nisbet, 1985; Klein, 1991; Baird et al., 1995; Naimark and Ismail-Zadeh, 1995]; and (4) dynamic topography

driven by large-scale mantle convection or isolated convective instabilities [e.g., *Middleton, 1989; Hartley and Allen, 1994; Downey and Gurnis, 2009*].

Some authors have proposed models in which a combination of two or more of these processes acts together, or at different times during basin evolution, for example, extension coupled with buried loading [e.g., *Hamdani et al., 1991, 1994; Stel et al., 1993*], buried loading and in-plane stress variations [e.g., *Howell and van der Pluijm, 1999*], extension and dynamic topography [e.g., *Armitage and Allen, 2010; Crosby et al., 2010*].

Many of these models would be expected to produce identifiable geological structures as well as distinct crustal structure and gravity anomalies. However, there is limited data on the deep structure of cratonic basins with which to constrain, compare, and contrast model predictions. Two basins that have previously been investigated using active source seismic techniques are the Williston and Michigan basins of North America. Beneath the Williston basin center, *Baird et al. [1995]* imaged several westward dipping reflections within the crust, which in places reach depths of ~60 km and therefore appear to extend into the mantle. However, they noted a distinctive absence of a reflection Moho, at odds with the well-imaged Moho in the central Saskatchewan region at the northern edge of the basin [e.g., *Morel-à-l'Huissi et al., 1987*]. The dipping reflectors were interpreted as a Hudsonian Orogeny structural fabric developed in the Paleoproterozoic (~1.8 Ga). The missing Moho was then attributed to the absence of any appreciable impedance contrast due to gradational eclogitization of a remnant Hudsonian crustal root beneath the basin. Beneath the Michigan basin center [*Zhu and Brown, 1986*] imaged an ~12 km thick reflective succession in a narrow ~70 km wide rift basin, the Midcontinent Rift, interpreted as a volcanoclastic sequence of upper and Middle Keweenawan age ~1.1 Ga [*Van Der Voo and Watts, 1978*]. They also imaged a potential Moho reflection at ~43 km depth, a result that has recently been corroborated by EarthScope receiver function studies [*Shen et al., 2013*].

In both Williston and Michigan, the crust has clearly been profoundly modified by pre-basin formation events making it difficult to distinguish between these structures and those potentially related to formation of the overlying cratonic basins. However, an important observation is that neither basin shows evidence of appreciable crustal thinning nor rift related structures, as one may expect for a rift origin.

In this paper, we examine the Parnaíba cratonic basin, located in Northeast Brazil. This basin was selected because it exhibits many of the characteristics of cratonic basins, including a subcircular shape, offlap of sediments at the basin edges and younging toward the basin center, a long history of sediment accumulation, and an association with thick lithosphere far from plate boundaries. This study is part of the Parnaíba Basin Analysis Project (PBAP), instigated by BP and the Agência Nacional do Petróleo. Central to this project was the acquisition of a regional ~1400 km, 20 s two-way travel time (TWTT) seismic reflection profile by Global Geophysical. Our database also includes coincident potential field (gravity and magnetic) data, industry seismic reflection lines, and well log data from >40 exploration wells and 58 hydrology wells [*Companhia de Pesquisa de Recursos Minerais (CPRM), 2016*]. We present here an analysis of these data. Firstly, the crustal structure is constrained along the seismic profile using seismic reflection, wide-angle reflection/refraction and potential field data. Next, we analyze the subsidence history of the basin by carrying out one-dimensional Airy-type backstripping of well log data and three-dimensional flexural backstripping of sediment isopachs. We then use these observations as constraints to test modes of basin formation. Our results show that the newly acquired data cannot be explained in terms of a rift origin for the basin. A better model that is in accord with all the available seismic, gravity, and well data is one in which the lower crust has been intruded by a magmatic body which loads the crust (and lithosphere), thereby causing a surface flexure into which sediments have been able to accumulate over long periods of geological time.

## 2. Geological Setting

The Parnaíba Basin (Figure 1) of Northeast Brazil is one of five cratonic basins within the South American plate. It is located above a complex basement comprising several Archaean and Proterozoic terranes that stabilized during the Brasiliano orogeny [e.g., *Cordani, 1984; Cordani et al., 2009; de Brito Neves et al., 1984; Fetter et al., 2000*]. The Phanerozoic basin largely conceals the boundaries between these terranes and their precise distribution (Figure 1). However, the seismic facies interpretation of *Daly et al. [2014]* and the potential field work of *de Castro et al. [2014]* have demonstrated the three dimensional form of these boundaries, enabling the definition of distinct crustal terranes with abrupt and apparently steep boundaries. The basin spans a subcircular area of some 670,000 km<sup>2</sup>. Its edges are erosional, suggesting that it may have once

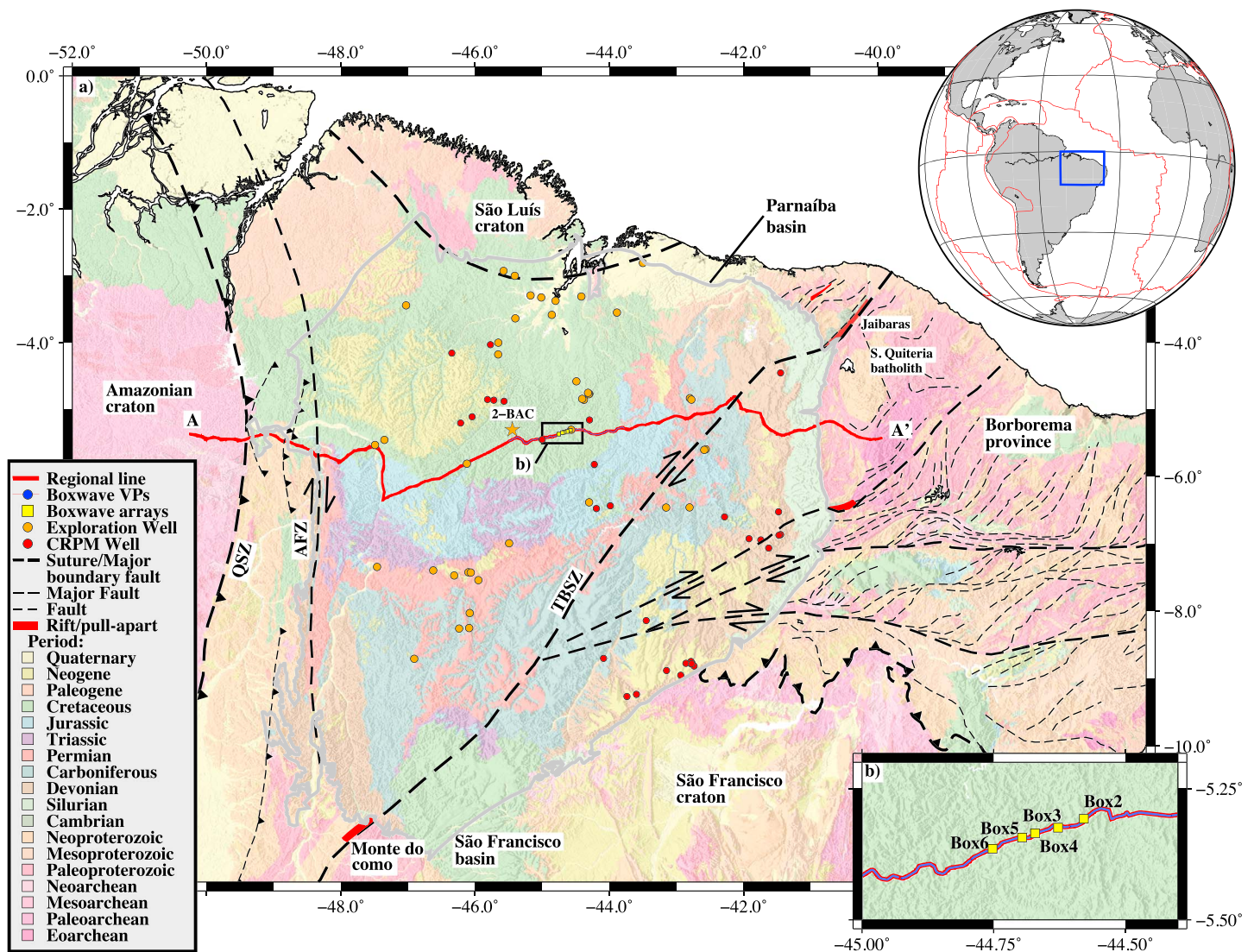


**Figure 1.** Geological setting of the Parnaíba cratonic basin, Northeast Brazil. Solid grey line shows the areal extent of the basin. Red line shows the PBAP seismic reflection profile. Orange filled circles show the locations of exploration well data. Inset top right shows bounding box of Figure 1a. Inset lower right shows the box wave survey geometry. Yellow stars show the location of the box wave receiver gathers. Dashed lines show principal tectonic features. AFZ = Araguaina Fault Zone, TBSZ = Transbrasiliano Shear Zone [Daly et al., 2014], and QSZ = Quatipuru Suture Zone. Fault locations in the Borborema Province are based on Ganade de Araujo et al. [2014a]. Geological map modified from Bizzi et al. [2003].

extended over a wider region, as evidenced by the presence of small outlier basins both to the west [Daly et al., 2014] and east [de Matos, 1992] of the basin. Furthermore, the Palaeozoic Saltpond Basin, located along the Ghana coast [e.g., Atta-Peters et al., 2015], appears to be a stratigraphic equivalent of Parnaíba and may once have been contiguous with Parnaíba prior to breakup of South America and Africa in the Upper Albian ~105 Ma [e.g., Moulin et al., 2010].

Like many cratonic basins, Parnaíba displays a polyphase sedimentary history. Five distinct tectonostratigraphic (TS) units are recognizable and are separated by basin-wide unconformities (Figure 2) [e.g., de Castro et al., 2014, 2016]. We term these units here the Riachão (TS-1), Jaibaras (TS-2), Parnaíba (TS-3), Mearim (TS-4), and Grajau (TS-5).

The Riachão unit (TS-1) includes the oldest preserved sediments in the basin. These sediments are believed to be Late Neoproterozoic to Cambrian in age [Mesner and Wooldridge, 1964; Porto et al., 2016] and are recorded from seismic and well data in the southwestern area of Parnaíba. de Castro et al. [2014, 2016] interpreted the Riachão package as a Neoproterozoic rift. However, this view has recently been challenged

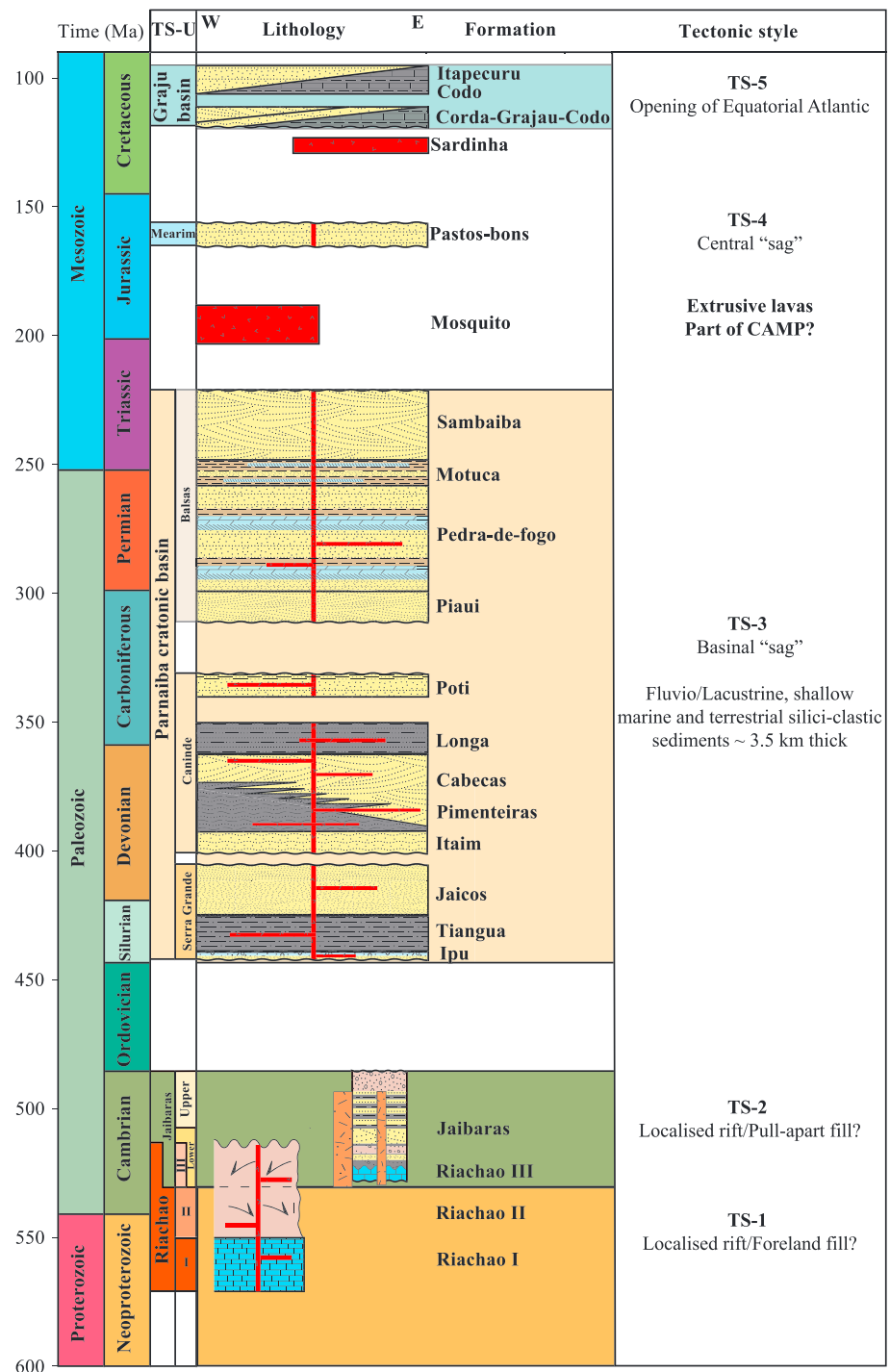


**Figure 2.** Summary stratigraphic column for the Parnaíba cratonic basin illustrating the main tectonostratigraphic (TS) units, lithologies, major unconformities, and regional tectonic events. TS-1 to TS-3 all reside above crystalline basement. Based on Vaz *et al.* [2007] and de Oliveira and Mohriak [2003].

by Porto *et al.* [2016], who, on the basis of industry two-dimensional seismic data and two wells, interpreted the Riachão as a remnant foreland basin, bounded by thick skinned thrust faults of Cambro-Ordovician age. Unit TS-2 comprises the volcanic dominated Jaibaras Group [de Sousa, 1996; Milani and Zalan, 1999]. This sequence outcrops within the graben-like Jaibaras and Monte do Carmo troughs, adjacent to the TBSZ at the northeast and southwest edges of Parnaíba basin, respectively (Figure 1). The equivalent sequence is

also seismically imaged and drilled adjacent to the TBSZ beneath the basin [de Castro *et al.*, 2016]. The Jaibaras Formation is interpreted as a rift infill resulting from a pervasive Cambro-Ordovician rifting event [e.g., de Oliveira and Mohriak, 2003]. However, the long (~50 km) and narrow (~15 km) form, NE/SW alignment and spatial association of these rifts with the TBSZ, leads us to believe they are more likely of a pull-apart origin, formed during dextral strike-slip motion along the TBSZ during the Cambrian/Early-Ordovician.

Unit TS-3 spans the Late Ordovician-Early Triassic and is the product of the cratonic basin subsidence being studied here. This unit consists of three megasequences, separated by regional unconformities and comprising shallow marine, fluviolacustrine, and terrestrial siliciclastic sediments that reach a maximum thickness of ~3.5 km in the center of the basin.

The oldest megasequence of the cratonic basin is the Serra Grande, spanning Early Silurian to Lower Devonian. It rests unconformably above crystalline basement and Cambrian sediments of the Riachão and Jaibaras Formations and consists of quartz arenites of fluvioglacial, glacial marine, and shallow marine sediments that account for a complete transgressive/regressive cycle [Milani and Zalan, 1999; de Oliveira and Mohriak, 2003]. A regional unconformity marks the termination of the Serra Grande and given its timing and has tentatively been related to far-field deformation during the Caledonian orogeny [e.g., Góes *et al.*, 1993]. The Serra Grande is overlain unconformably by the Caninde megasequence, which spans the Lower Devonian-Carboniferous. It comprises interbedded shallow marine and deltaic depositional environments with little change in depocenter location with respect to the Serra Grande [e.g., Góes *et al.*, 1993; Trindade *et al.*, 2015]. A Late Carboniferous regional unconformity marks the termination of the Caninde megasequence. This hiatus has been attributed to far-field inversion driven by the Hercynian orogeny [Góes *et al.*, 1993], which was active along the northwestern coast of Africa at this time.

The Late Carboniferous to Middle Triassic Balsas is the youngest megasequence, believed to mark the terminal stage of Parnaíba cratonic basin subsidence. It comprises clastic sandstones and evaporites deposited in subaerial environments [e.g., Góes and Feijó, 1994; Milani and Zalan, 1999].

A Middle Triassic unconformity seals the underlying Parnaíba cratonic basin stratigraphy. This is marked along the western side of the basin by a phase of predominantly extrusive volcanism, with the deposition of basaltic lava flows known as the Mosquito Formation [Góes *et al.*, 1993; Merle *et al.*, 2011]. The basaltic interval is up to ~200 m thick and  $^{40}\text{Ar}/^{39}\text{Ar}$  dating suggests ages of  $199.4 \pm 2.7$  Ma [Merle *et al.*, 2011]. Their origin is attributed to the Central Atlantic magmatic province, which is related to formation of the East Coast, USA, and West Africa rifted margins and the opening of the central Atlantic Ocean [e.g., Baksi and Archibald, 1997].

The Late Jurassic Mearim Unit (TS-4) overlies the Mosquito volcanics. It contains sediments of the Pastos Bons Formation deposited in a sabkha environment [e.g., Góes *et al.*, 1993; Araujo *et al.*, 2016] and is restricted to the center of the basin.

Subsequent to Mearim sedimentation, a second phase of basaltic magmatism took place during the Middle Cretaceous. These volcanics, known as the Sardinha Formation, have a high-Ti composition and are found mostly in the northeast portion of the basin, with individual sills up to 400 m thick. Merle *et al.* [2011] determined  $^{40}\text{Ar}/^{39}\text{Ar}$  and K/Ar whole-rock ages for the sills of ~129–124 Ma and attributed them to magmatism associated with the early opening of the South Atlantic Ocean.

The youngest Unit (TS-5) is the Cretaceous Graju subbasin. This unit unconformably overlies the Parnaíba and Mearim Units. It comprises the Corda, Grajau, Codo, and Itapecuru Formations, which consist of near-shore, shallow marine, and fluviolacustrine clastic sediments, respectively. This phase of deposition has been attributed to subsidence associated with early opening of the South Atlantic [e.g., Rossetti *et al.*, 2004]. Tertiary and Recent fluvial deposits also outcrop locally within the basin.

### 3. Geophysical Data

#### 3.1. Regional Seismic Reflection Profile

The poststack depth migrated PBAP seismic reflection profile is shown in Figure 3 and as a poststack time migrated profile in Figure S1. The profile is based on the same data as discussed in Daly *et al.* [2014]; however, an additional poststack semblance smoothing coherency filter [Milkereit and Spencer, 1989] has been applied to the stack in order to enhance the deep crustal reflectivity. A further difference is that we have removed the section of the profile that trends north-south, located ~47.5°W. Additionally, the data

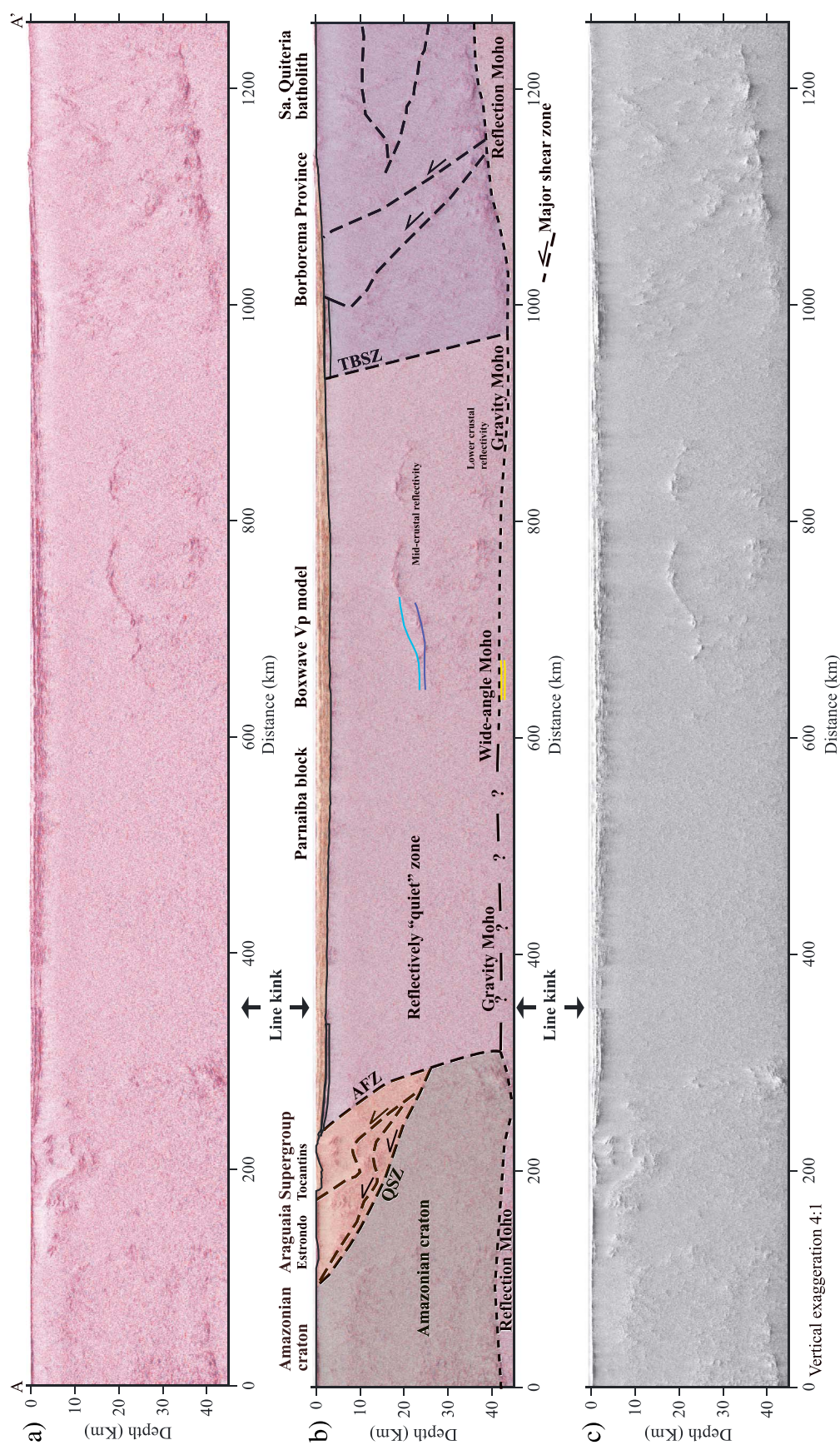


**Figure 3.** (a) Poststack depth migrated seismic reflection profile with coherence filter applied. A–A' shown in Figure 1. Note the line kink at ~47.5°W (Figure 1) has been removed. (b) Same as in Figure 3a with interpretation overlain (modified from Doly *et al.* [2014]). AFZ, QSZ, and TBSZ are as defined in Figure 1. (c) Same as in Figure 3a but displayed using amplitude relief.

**Table 1.** Comparison of Box Wave and MCS Acquisition Parameters (Modified After *Daly Et Al.* [2014])

Parameter	Seismic Reflection Profile	Box Wave Survey	Units
Receiver interval	50	~ 5000	m
Source interval	50	50	m
Maximum offset	$\pm 12$	$\pm 110$	km
Record length	20	40	s
Number of sweeps	2	2, 4, 8, 16	-
Sweep length	24	40	s
Sweep frequency	6–60	4–32	Hz
Peak force/vibrator	27,200	27,200	kg
Total force/sweep	108,800	108,800	kg
Fold	240	Low (1–8)	-
Number of vibrators/fleet	4	4	-

are displayed as an amplitude relief plot, which further aids in the identification of deep reflections and the sedimentary/basement contact. The seismic data acquisition parameters are listed in Table 1.

The Amazonian craton in the west is characterized by flat-lying reflections within the upper crust and a Moho depth of ~40–42 km. Basinward, a highly complex pattern of reflections in the upper part of the crust is observed with a general eastward dip, defining the Araguaia belt metasediments of the Tocantins and Estrondo groups, which were obducted northwestward along the Quatipuru Suture Zone (QSZ, Figure 3) during Brasiliano orogenesis [*Alvarenga et al.*, 2000; *Moura et al.*, 2008]. Beneath this package, the Moho dips basinward, deepening locally to ~44.5 km [*Daly et al.*, 2014]. This is indicative of a crustal flexure driven by the emplacement of Araguaia fold and thrust belt load as proposed by *Ussami and Molina* [1999].

Farther eastward, reflectivity terminates abruptly. This contrast marks the crustal expression of the Araguaia Fault Zone (AFZ, Figure 3), where at the surface, late stage Brasiliano north-south dextral strike-slip displacement was accommodated [*Fonseca et al.*, 2004]. The AFZ marks the boundary between the Araguaia Supergroup and the western section of the Parnaíba block, which appears acoustically featureless on this profile. The eastern section, however, is characterized by a prominent zone of midcrustal reflectivity (MCR) at depths between ~17 and 25 km and an ~12–18 km thick reflective lower crust. The Moho is not easily identified in the basin center. Originally, the base of the high-amplitude reflections at model km 780 was interpreted as Moho. However, between model km 680 and 750 these reflections exhibit an eastwardly dip, shallowing to ~28 km depth. This is much shallower than the Moho depth of ~42 km determined by gravity and *P* wave velocity modeling (as discussed in the following sections), and hence, these reflections appear to occur within the lower crust.

Further east, another abrupt change in the seismic facies occurs. This is interpreted as the crustal expression of the Trans-Brasiliano Shear Zone (TBSZ), separating the Parnaíba block from the Borborema province. The Borborema province is characterized by extensive crustal scale shear zones, with apparent easterly dips of ~20–30°. These appear to sole into a well-resolved reflection Moho, which steadily deepens basinward from ~35 km at the profile edge to ~44 km at its intersection with the TBSZ.

Parnaíba Basin resides primarily upon the Parnaíba block but also extends onto the Amazonian Craton and Borborema Province to the west and east, respectively. Within the regional seismic reflection profile, the basin exhibits the simple bowl-shaped sag geometry and “layer-cake” stratigraphy typical of cratonic basins. Given that some authors postulate cratonic basins form by extension and represent the low strain rate end-member of rift-type basins [e.g., *Armitage and Allen*, 2010; *Allen and Armitage*, 2011; *Cacace and Scheck-Wenderoth*, 2016], it is significant that we find little evidence for extensional strain within the sedimentary basin or basement, with no appreciable normal faults observed and no central rift graben imaged. This implies that if extension is responsible for basin formation, then it must be expressed in a manner that differs from the brittle normal faulting commonly observed at rift basins. For example, *Armitage and Allen* [2010] speculated, assuming a rift origin, that at the low strain rates implied by the longevity of cratonic basin subsidence, extension may be accommodated in some diffusive manner, such that it is not resolved in seismic imaging. However, as discussed by *Holt et al.* [2015], analogue models [*Bellahsen et al.*, 2003] and field observations [*Mazzarini et al.*, 2004] suggest that at low strain rates, extension is more likely to become localized on fewer, large faults. Therefore, it appears that an extensional origin is inconsistent with Parnaíba Basin seismic structure, and an alternative mechanism must be responsible for basin subsidence.

and possibly cratonic basins in general [e.g., *Stel et al.*, 1993; *Hamdani et al.*, 1991, 1994; *Sleep*, 2009; *Holt et al.*, 2010, 2015; *McKenzie and Priestley*, 2016].

### 3.2. Box Wave Receiver Gathers

During the acquisition of the PBAP reflection profile, five wide-angle split-spread receiver gathers were collected near the center of the basin, with maximum offsets of  $\pm 110$  km (Figure 1). These data were acquired using modified source and receiver parameters, designed to record long offset, wide-angle reflections and refractions (see Table 1). Specifically, a lower minimum sweep frequency of 4 Hz was used, and the gathers were collected in the common receiver domain (as opposed to the common shot domain) using an areal receiver array (Figure 4a).

The arrays each consisted of 225 receiver nodes deployed as  $280 \times 280$  m grids with 20 m spacing between each node (Figure 4a). Given their shape, arrays of this type are known as “box wave” arrays [Regone, 1997]. Such arrays suppress noise in two ways: first, by stacking the signal recorded at each node, incoherent noise is suppressed by a factor of up to  $\sqrt{n}$  (where  $n$  is the number of receiver traces), in a similar manner to common-depth-point stacking. Second, low-velocity coherent noise is also suppressed, as the array effectively works as a spatial wave number filter [e.g., *Holzman*, 1963; *Regone*, 1997]. As low-velocity surface waves arrive with near-horizontal incident angles, they exhibit apparent higher wave numbers and are rejected (add destructively), while the desired signals (reflections and refractions) typically arrives at higher incidence angles, exhibiting lower apparent wave numbers, and are passed (add constructively) when the signals are stacked (Figure 4c). This was particularly useful for this survey as Rayleigh surface waves (ground roll) generated by the Vibroseis signal and road traffic had a detrimental effect on data quality. The array geometry used, coupled with a Chebychev trace weighting scheme [Holzman, 1963], theoretically provided a suppression of  $\sim 46.5$  dB for wave numbers within the reject band (Figure 4b).

Figure 5 shows the receiver gather acquired at Box 2 (Figure 1). The gathers for Boxes 3–6 are shown in the supporting information Figures S2–S5. The box wave gathers exhibit a far superior data quality in comparison with the standard shot gathers acquired along the PBAP seismic reflection profile. However, dispersive surface waves are still prevalent on the near-offset traces ( $< 35$  km) and degrade deep reflections at wider offsets (Figure 5).

Nevertheless, clear  $P$  wave ( $V_p$ ) arrivals are observable on all five box wave gathers, and we pick four prominent arrivals for travel time modeling ( $P_g$ ,  $P_cP$ ,  $P_i$ , and  $P_mP$ ). First arrival refractions from within the sedimentary basin and uppermost crust ( $P_g$ ) are observable out to maximum offsets of  $\sim 30$  km and were used to constrain upper crustal velocities.

Most prominent is an  $\sim 5.3$  s thick package of continuous to semicontinuous reflections from  $\sim 8.5$  to 13.8 s. The reflection from the top of this package ( $P_cP$ ) extends to offsets of  $\sim 35$ –45 km both east and west and reappears as a strong reflection to the east at offsets of  $\sim 50$ –100 km. The poor data quality at offsets between  $\sim 35$  and 50 km is likely the result of interference with the dispersive surface wave energy that intersects the  $P_cP$  phase at these offsets.

On the eastern side of the gathers, a prominent linear arrival is evident above the  $P_cP$  reflection at offsets  $> 55$  km ( $P_i$ ). We interpret this as a refracted head wave from an interface related to that which produces the  $P_cP$  reflection.

At the base of the reflectivity package, we pick the latest arriving, laterally coherent reflection phase ( $P_mP$ ) and interpret this as the reflection Moho [e.g., *Cook*, 2002]. This reflection is identifiable to offsets of  $\sim \pm 35$  km.

Given the modest data volume of our wide-angle reflection/refraction data set, we chose to forward model the  $V_p$  crustal structure using the ray tracing method of *Zelt and Smith* [1992]. This approach allows greater control over model parameters and incorporation of constraints from the seismic reflection profile and gravity modeling results. Within the model, each layer is defined by an arbitrary number of boundary and velocity nodes connected by linear interpolation and modeled arrival times are derived by tracing rays through the model. Misfits between the calculated and observed travel times were reduced by manual adjustment or damped least squares inversion of specific model parameters.

We constructed the model using a “top-down” and “prior-structure” approach [Zelt, 1999]. Interval velocities derived during processing of the regional reflection profile [Daly et al., 2014] were used to constrain  $V_p$  within the sediment basin and held fixed during modeling of the deeper structure. This is important, as errors in

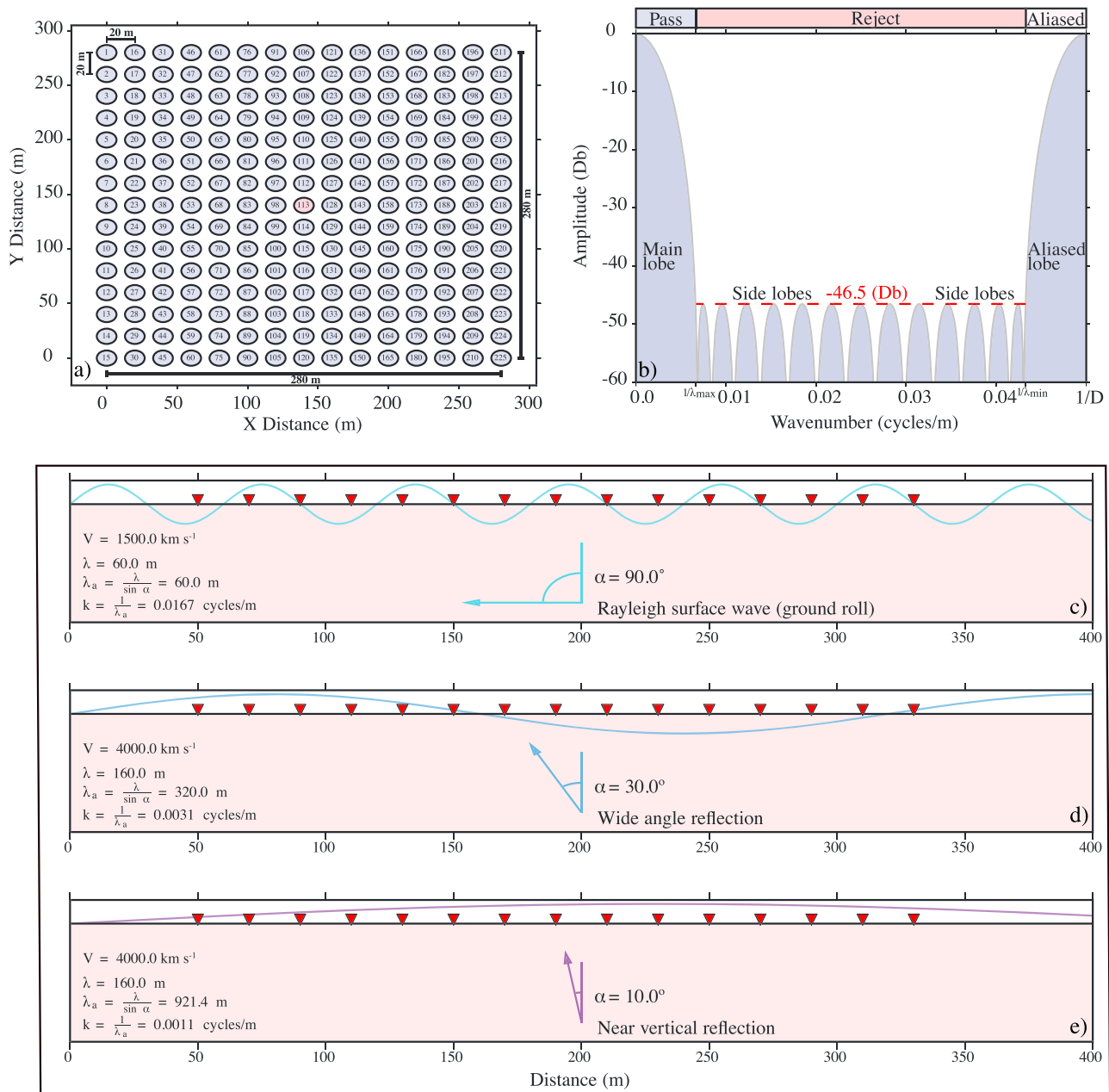


**Figure 4.** (a) Schematic layout of the box wave areal receiver array used to acquire the five receiver gathers analyzed in this study. Blue circles represent receiver nodes. Note the location of the central receiver node (113) is the geographic location of the receiver gather, with trace offsets measured relative to this. (b) Array response diagram showing the theoretical attenuation achieved using the areal array shown in Figure 4a and a Chebychev weighting scheme [Holzman, 1963] with respect to the signal that would be recorded by an equal number of geophones placed at single location [e.g., Sheriff and Geldart, 1995]. (c–e) Schematic illustrations showing the dependence of apparent wavelength on emergence angle (modified after Pap [1983]). Note that as emergence angle decreases, the apparent wavelength approaches infinity.

these low velocities can result in large travel time errors propagating into deeper sections of the model, producing large errors at interface depths [e.g., Stern et al., 2010].

Assessment of the goodness of fit is performed by statistical analysis of a travel time misfit using root-mean-square (RMS) and normalized chi-square ( $\chi^2$ ) values as well as ray density analysis and residual travel time versus offset visualization. Model nonuniqueness and uncertainties are estimated by performing  $V_p$  perturbation tests,  $V_p$  inversion recovery tests and parameter grid search tests on selected parameters (Figures S6–S11) and by using a bounded Monte Carlo method to explore a larger parameter space (Figures 6e and 6f).

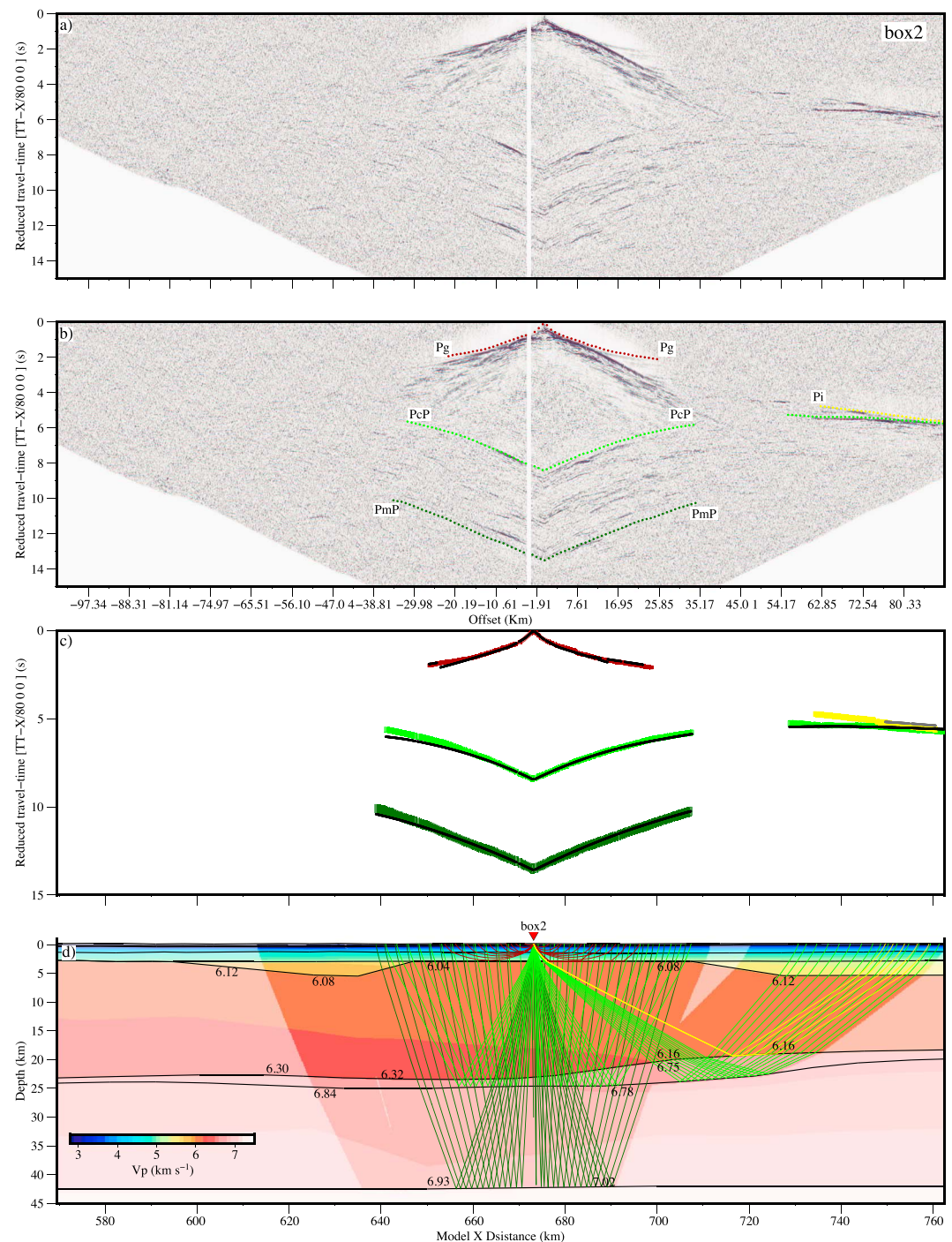


**Figure 5.** (a) Box 2 receiver gather with signal processing applied to aid in phase identification. We have applied an FK filter, FX-deconvolution, and sembsmooth coherency filters, predictive deconvolution; a [2–4–12–15] Hz band-pass filter; full trace balance and 3000 ms AGC. (b) Same as above but with picked phase interpretations shown. (c) Picked (colored) and modeled (black and grey ( $P_i$ )) travel time arrivals. (d) Modeled crustal  $V_p$  structure with a subset of ray paths from each phase. Numbers are  $V_p$  in  $\text{km s}^{-1}$ . Transparent mask indicates regions unsampled by rays.

$P_g$  refraction arrivals constrain upper crustal  $V_p$  with values between 6.04 and 6.12  $\text{km s}^{-1}$ . Given these only sample the top of the upper crust, a 1-D velocity gradient was assumed and a parameter search method was used to determine which combinations of  $V_p$  gradient and interface depth provide an adequate fit to the  $P_cP$  reflections, while holding the geometry of the MCR determined from the regional reflection profile fixed (Figure S10).

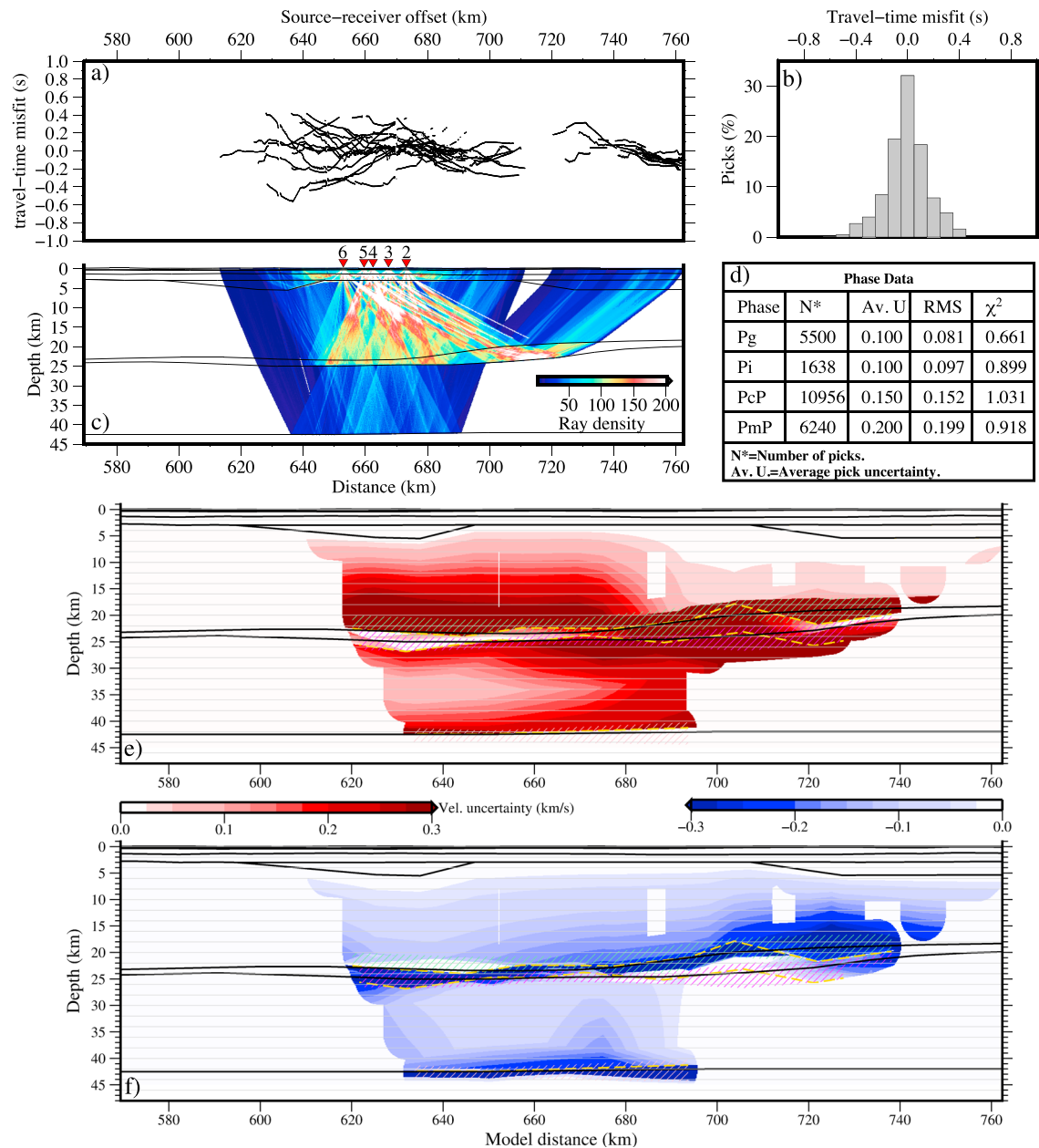


**Figure 6.** (a) Travel time residuals for all modeled rays plotted against true receiver locations. (b) Same data as in Figure 6a plotted as a percentage histogram, binned in 50 ms intervals. (c) Ray hit count computed using 200 × 200 m grid cells. Dashed black lines are model layers and inverted red triangles locate box wave data sets 2–6. (d) Model statistics for each picked phase group. (e and f) Maximum allowable  $V_p$  variations from the final model values derived from Monte Carlo uncertainty analysis. Black lines are layer interfaces from the final forward model. Dashed yellow lines are interface depths that provide the best fit within Monte Carlo limits. Colored dashes show maximum depth variation for each model interface.

The resulting model provided an excellent fit to the  $PcP$  arrivals; however, an acceptable fit of the observed  $Pi$  refraction arrivals was not possible with this geometry. We found from forward modeling that the  $Pi$  arrivals require a shallower interface than the  $PcP$  reflections, which reflect from an interface approximately ~2–3 km deeper and parallel to the refraction interface. These two layers then define a midcrustal zone, consistent with approximately the top and base of the ~3 km thick band of reflectivity that defines the MCR on the regional reflection profile (Figure 3).  $V_p$  in the upper crustal section appears slightly lower than the global average for shields and platforms [Christensen and Mooney, 1995] and reaches a maximum of  $6.30 \text{ km s}^{-1}$  at a depth of ~23 km.

In order to fit the gradient of the  $P_i$  refraction phase, the lower layer requires a large increase in  $V_p$  to  $6.75 \text{ km s}^{-1}$ , consistent with a large acoustic impedance contrast evident by the high amplitude of the MCR on the regional reflection profile.

In the absence of any lower crustal refraction arrivals, a 1-D  $V_p$  gradient was assumed for the lower crust and the  $PmP$  arrivals were modeled as originating from the Moho. Again, we use a grid search approach to test which combinations of  $V_p$  gradient/interface depth provide an adequate fit to the travel times (Figure S11). This shows an inherent trade-off between interface depth and  $V_p$  gradient; however, the travel time misfit only resides within our pick error (200 ms) along a narrow band, constraining the depth to Moho of  $42 \pm 1 \text{ km}$ .

Once the model was constrained within an acceptable misfit, we inverted for best fits to the upper and lower crustal layers using damped least squares. Three-point median smoothing was applied between inversion iterations to prevent the development of large  $V_p$  gradients and inversions were run until the updated model failed a statistical  $F$  test for significant difference at the 5% confidence level [e.g., Zelt and Smith, 1992].

Due to the reverberant nature of the box wave gathers, travel time picks were assigned relatively large uncertainties of 100, 150, 150, and 200 ms for the  $P_g$ ,  $PcP$ ,  $P_i$ , and  $PmP$  phases, respectively. Given these uncertainties, the majority of travel times are modeled within reasonable  $\chi^2$  bounds. The overall RMS misfit for the model is 0.162 s and  $\chi^2$  1.079, with individual  $\chi^2$  values range between 0.081 and 6.306 and the vast majority between 0.5 and 1.5.

Figure 6a shows most travel time residuals are within  $\pm 200 \text{ ms}$ , and no large outliers exist. There is also no strong correlation between high residuals and a particular region of the model. Furthermore, Figure 6b shows that there is no strong bias toward positive or negative residuals. Individual phase statistics are listed in Figure 6d.

A limitation of the model is the inability to trace arrivals to observations of the nearest offset  $P_i$  head waves observed on the Box 2 gather (Figure 5). These arrivals can be well fit if they are modeled as a reflection phase from an interface located  $\sim 2 \text{ km}$  above the  $P_i$  interface and dipping steeply to the east; however, given that no structure of this nature is imaged on the seismic reflection profile (Figure 3), we prefer a head wave interpretation.

Although the box wave survey consists of a relatively small data volume, the narrow station spacing of  $\sim 6 \text{ km}$  produces ray sampling overlap, providing data redundancy for the estimates of interface depths (Figure 6c). The model is best sampled between model coordinate 640–690 km where  $P_g$ ,  $PcP$ , and  $PmP$  rays from multiple gathers sample the upper most, middle crust, and lower crust, respectively. The MCR is also well sampled by wide-angle reflections between model coordinates 700–725 km.

To assign uncertainties to model parameters, we used a bounded Monte Carlo approach to generate 60,000 random models using the method of Loureiro *et al.* [2016]. The sedimentary basin layers and upper most crustal  $V_p$  nodes (constrained by the regional reflection profile and  $P_g$  refractions) were held fixed. The remaining model parameters were allowed to vary within specified bounds. Velocity and depth nodes were allowed to vary by  $\pm 0.30 \text{ km s}^{-1}$  and  $\pm 3.0 \text{ km}$  with respect to the final forward model. These values were chosen, as it was found that simulations with larger limits failed to find models capable of adequately fitting the data. Models which were capable of tracing  $\geq 95\%$  of rays and with an overall RMS misfit  $\leq 115\%$  of the final forward model (0.179) were used to assign uncertainties. Figures 6e and 6f show that the maximum acceptable  $V_p$  deviations from the final model and indicate bulk  $V_p$  values are constrained within  $< \pm 0.250 \text{ km s}^{-1}$ . Large  $V_p$  uncertainties occur at layer interfaces. However, these are artifacts due to large  $V_p$  discrepancies that arise when comparing models that place different layers (with large  $V_p$  differences) at the same depth [Loureiro *et al.*, 2016]. Dashed yellow lines show the best fit layer interfaces. The  $P_i$  and MCR interfaces have large uncertainties due to the velocity-depth trade-off surrounding these layers. The Moho interface is constrained to a depth between 41 and 44 km.

### 3.3. Low-Fold Reflection Stack

A low-fold unmigrated common depth point reflection stack was created by stacking all five box wave receiver gathers (Figure 7). This was performed for comparison with the regional reflection profile, principally to assess the spatial extent of the MCR and the nature of the lower crust and Moho. In order to exaggerate the lower crustal and Moho reflections, we applied semblance smoothing [Milkereit and Spencer, 1989] and FX deconvolution spatial coherency filters prestack and FX deconvolution again poststack and display these data using instantaneous amplitudes [Taner and Sheriff, 1977]. Full processing details are listed in Table S1.

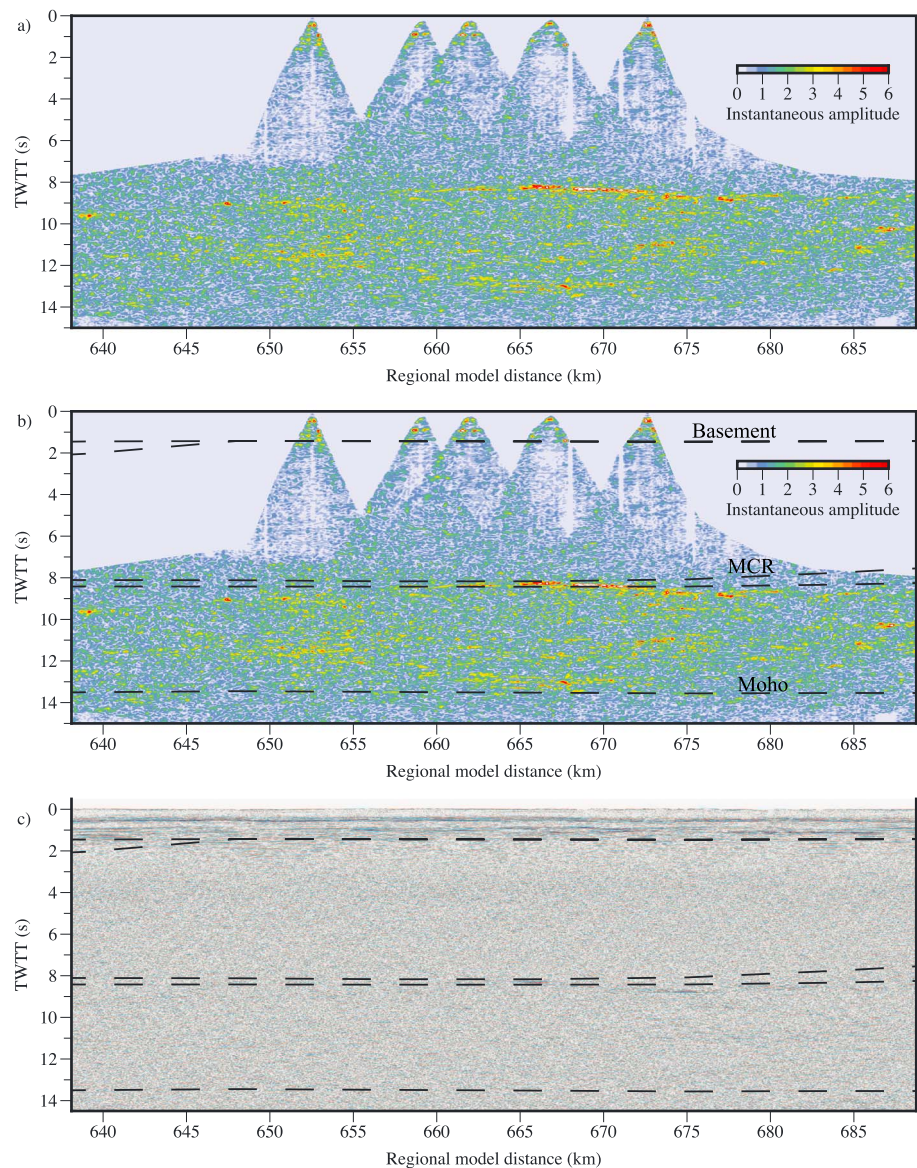


**Figure 7.** (a) Unmigrated low-fold seismic reflection stack of the five box wave wide-angle receiver gathers displayed using instantaneous amplitude [e.g., *Taner and Sheriff, 1977*]. (b) Same as in Figure 7a but with depths of the basement, MCR, and Moho interfaces from the  $V_p$  model converted to two-way travel time overlain (dashed lines). Note the good agreement of the basement and MCR, while the Moho appears slightly shallower on the stack. (c) Regional reflection profile with same interfaces as in Figure 7b overlain.

As shown in Figure 7a, reflections are best resolved directly beneath Boxes 2–6, where on the raw gathers deep reflections are also more easily identified (e.g., Figures 5 and S2–S5). The MCR is identifiable at  $\sim 8.5$  s TWTT and closely correlates with the MCR interface from the wide-angle  $V_p$  model when converted to TWTT (dashed lines in Figure 7b). It can be seen the MCR exhibits a relatively high amplitude, as would be expected from the large impedance contrast implied by our  $V_p$  model (Figure 5d). Several zones of high amplitude are visible beneath the MCR down to  $\sim 13.5$  s TWTT, and the base of this reflectivity is interpreted as Moho. A high-amplitude reflection at model km 670 and  $\sim 13.3$  s TWTT occurs slightly above the Moho interface derived from  $V_p$  modeling.

### 3.4. Gravity Anomaly Data

Gravity data were acquired at  $\sim 1$ – $2$  km interval, coincident to the seismic reflection profile. A total of 821 measurements were obtained using a Scintrex CG-5 land gravimeter and reduced to free-air gravity anomalies using the 1967 International Gravity Formula (flattening =  $1/298.25$ ). Bouguer anomalies were calculated

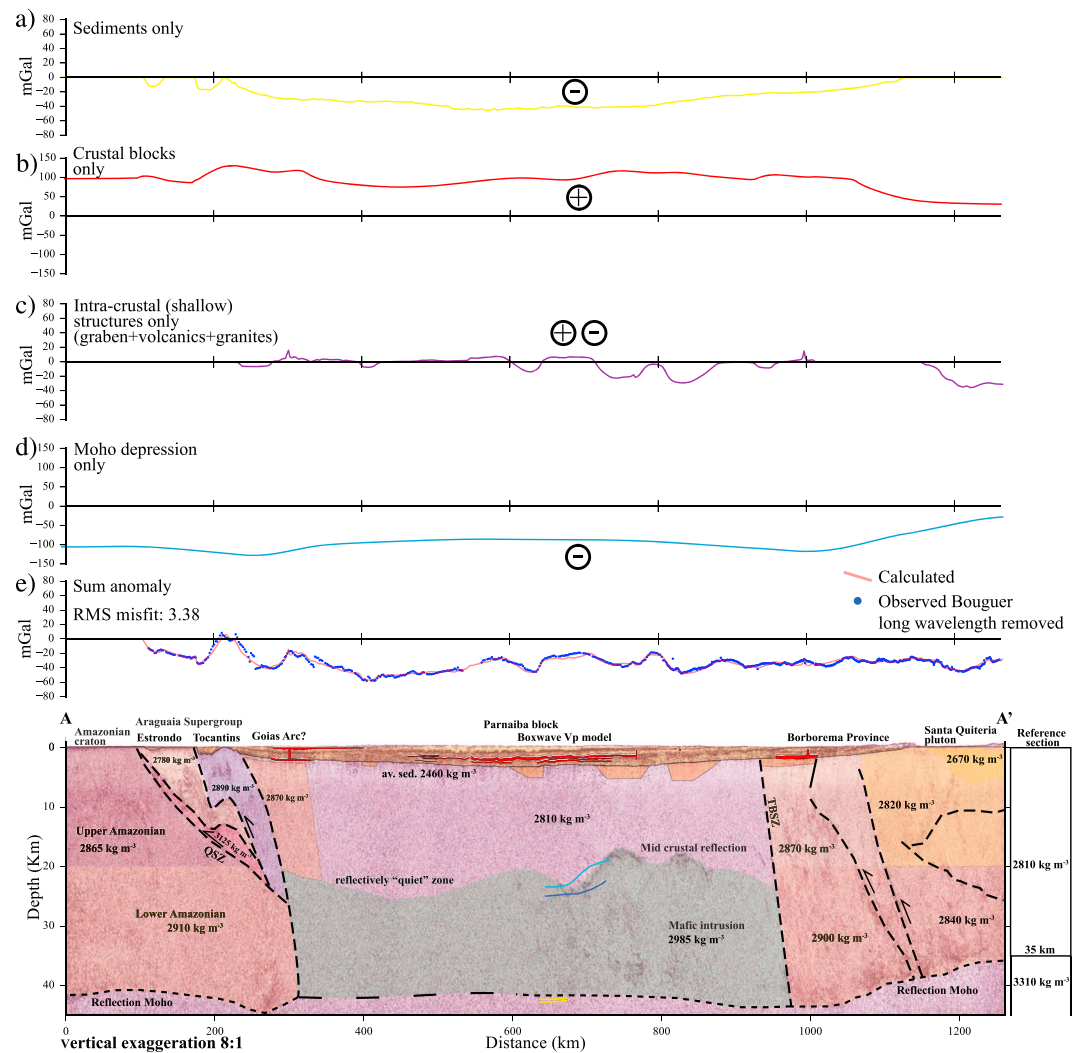


**Figure 8.** Comparison of observed and calculated Bouguer gravity anomalies along the PBAP seismic reflection profile. (a) Gravity effect of the sediments only. (b) Gravity effects of intracrustal structures only. (c) Gravity effect of the main crustal blocks. (d) Gravity effect of the Moho depression. (e) Comparison of observed and calculated Bouguer gravity anomalies. The observed anomaly (blue circles) has had the regional gravity field (to degree and order 12) removed. The calculated anomaly (red line) is based on the sum of Figures 8a–8d. (f) Crustal structure showing the depth converted seismic data and the body geometries and densities used in the gravity calculations. The reference section for the calculation of the density contrasts is shown to the right of the seismic profile. Colored lines are interfaces from the box wave  $V_p$  model shown in Figure 5d. av. Sed. = sediment density averaged over all formations.

using the planar slab formula and a reduction density of  $2650 \text{ kg m}^{-3}$ . The Bouguer anomalies were corrected for terrain using a Shuttle Radar Topography Mission digital elevation model [Farr *et al.*, 2007] and circular zones around individual stations, out to an outermost zone of 167 km. The correction was calculated using the prism method of Blakely [1995] as implemented by Cella [2015].

Prior to interpretation, we subtracted the long wavelength component of the EGM2008 gravity field model [Pavlis *et al.*, 2012] complete to degree and order 12 (equivalent to wavelength,  $\lambda$ , of  $\sim 3300$  km) from the terrain corrected Bouguer anomaly. We selected degree and order 12 since this field is dominated by the gravity highs associated, for example, with subducted slabs and the lows associated with late glacial rebound, which are unrelated to relatively shallow crustal structure.

The Bouguer gravity anomaly data show that Parnaíba Basin is associated with a broad “low” of  $\sim -40$  mGal (Figure 8). Superimposed on the low is a long wavelength ( $\lambda \sim 1200$  km) central gravity anomaly “high” of  $\sim +25$  mGal, with shorter wavelength ( $\lambda < 50$  km) localized lows of  $\sim 20$  mGal. The western edge of the basin,

**Table 2.** Summary of Parameters Used in the Thermal and Mechanical Modeling

Parameter	Symbol	Value	Units
Thermal thickness	$T_L$	170	km
Zero elevation crustal thickness	$T_\xi$	35	km
Crustal density at 0°C	$\rho_c$	2810	kg m <sup>-3</sup>
Mantle density at 0°C	$\rho_m$	3310	kg m <sup>-3</sup>
Water density	$\rho_w$	1030	kg m <sup>-3</sup>
Coefficient of thermal expansion	$\alpha$	$3.28 \times 10^{-5}$	°C <sup>-1</sup>
Mantle potential temperature	$T_p$	1333	°C
Thermal diffusivity	$\kappa$	0.008	cm <sup>2</sup> s <sup>-1</sup>
Stretching factor	$\beta$		
Crustal thermal conductivity	$K_c$	3.138	W m <sup>-1</sup> K <sup>-1</sup>
Lithospheric mantle thermal conductivity	$K_m$	3.138	W m <sup>-1</sup> K <sup>-1</sup>
Acceleration due to gravity	$g$	9.81	m s <sup>-2</sup>
Internal heat generation	HFC	0.0	HFU
Youngs modulus	$E$	100	GPa
Poissons ratio	$\nu$	0.25	-
Infill density	$\rho_{\text{infill}}$	1030	kg m <sup>-3</sup>
Sediment density (POGM)	$\rho_s$	2460	kg m <sup>-3</sup>
Buried load density (POGM)	$\rho_l$	2985	kg m <sup>-3</sup>

which is approximately coincident with the QFZ, is characterized by a local high with flanking lows to either side. While the eastern edge of the basin and the TBSZ do not correlate with any significant Bouguer anomalies. The ~15 mGal low at the extreme eastern end of the profile is attributed to the Santa Quiteria batholith, a Neoproterozoic granitic pluton.

We have used the gravity data measured along the reflection profile to verify the results from seismic modeling. Specifically, we used densities of sedimentary formations recorded in well logs, the depth converted regional seismic reflection profile (Figure 3b), the box wave wide-angle reflection model (e.g., Figure 5d), and consideration of the surface geology to constrain a 2-D density model along the PBAP profile. The gravity anomalies expected for this density structure were calculated and compared to the observed Bouguer anomaly with the long wavelength gravity field removed. We note that the velocity model used to perform post-stack depth migration of the regional reflection profile is not constrained below a depth of ~5 km, and hence, we did not fix our Moho and MCR interfaces to the exact reflection depths; instead, we used these estimates as a starting point for the density model and the gravity calculations. Moreover, given that the relationship between  $V_p$  and density is dependent on rock composition (which is unknown) the density model derived in Figure 8 was constructed independently from the  $V_p$  structure derived in Figure 5. Consistency between the final density and  $V_p$  values was tested by converting the final  $V_p$  values to densities using the empirically derived curves of *Ludwig et al.* [1970] and *Brocher* [2005] and comparing them to the final density values. This showed that the densities are within  $\pm 3\%$  of the average relationship given by the Nafe-Drafe curve and are also consistent with the values presented in the global data compilations of *Christensen and Mooney* [1995] and *Vacher and Souriau* [2001].

The gravity anomalies associated with the individual crustal bodies in Figure 8 were calculated using the *Talwani et al.* [1959] line integral method. Bulk densities for each sedimentary formation were assigned using the mean values from a suite of measurements located throughout the basin. Densities were modeled with respect to a “standard” reference column, determined by isostatically balancing a 35 km thick column of continental crust at zero elevation against a mid-ocean ridge crest column, assuming the thickness and density parameters in Table 2 [e.g., *Cochran*, 1981]. There is some uncertainty as to what value is most reasonable to assume as the reference crustal thickness in this setting; however, we have selected a reference of 35 km because it is in accord with the seismically constrained crustal thickness in onshore regions flanking Parnaíba Basin, which are typically in the range ~32–38 km (Figure 9) [e.g., *Assumpção et al.*, 2013; *de Lima et al.*, 2015; *Luz et al.*, 2015].

Figure 8 shows the individual contributions from the mass deficiency of the sediments and the thicker crust and the mass excess associated with the dense lower crust, together with the sum anomaly. The sum anomaly comprises two main negative contributions: one from the relatively low density sediments (~–45 mGal) and the other from the displacement of low-density crust into denser mantle (~–90 mGal). The combined

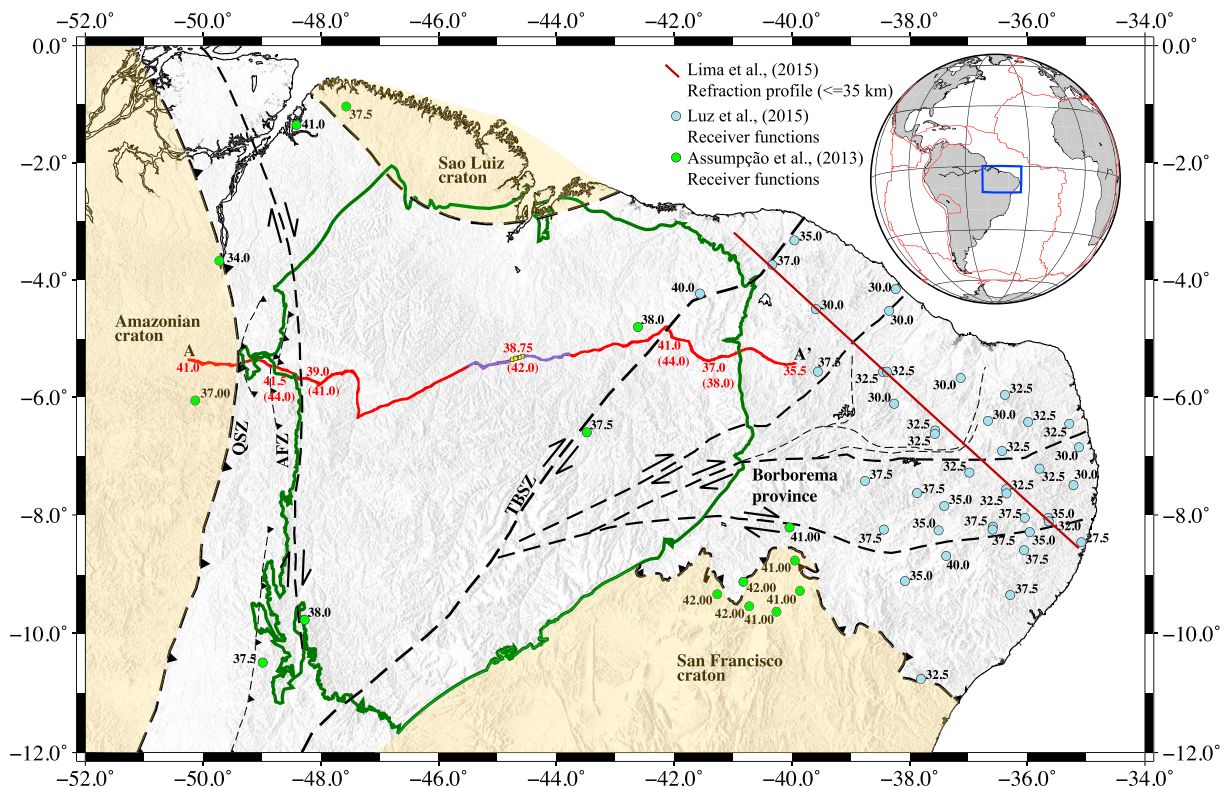


**Figure 9.** Crustal thickness estimates in and surrounding the Parnaíba cratonic basin, Northeast Brazil (dark green line). Text values are crustal thickness in kilometers. Red text values are those from data analyzed in this study (regional reflection profile and box wave receiver gathers). Dark red line is the active source reflection/refraction profile from *de Lima et al.* [2015]. Light blue circles are receiver function estimates from *Luz et al.* [2015]. Green circles are receiver function estimates from various studies, taken from the compilation of *Assumpção et al.* [2013]. Red line is the regional PBAP reflection profile from this study (Figure 3). Blue line shows the vibroseis points recorded at the box wave receivers (yellow squares) in the basin center. Cratons surrounding the basin are shaded yellow. Dashed lines show principal tectonic features. AFZ = Araguaia Fault Zone, TBSZ = Transbrasiliano Shear Zone [Daly et al., 2014], and QSZ = Quatipuru Suture Zone. Inset top right shows bounding box the main figure.

negative contribution amounts to some  $\sim -135$  mGal. The main positive contribution arises from the relatively high density lower crust (the upper surface of which is defined by the MCR) compared to surrounding regions and results in a positive anomaly of up to  $\sim +100$  mGal. The existence of an anomalously dense body in the lower crust of Parnaíba Basin has also been suggested by *de Sousa* [1996]. When the gravity effect of this mass excess is combined with the mass deficiency due to the sediments and crustal thickening, it yields a net gravity anomaly of  $-135 + 100 = \sim -35$  mGal, which is of similar amplitude to the observed Bouguer gravity anomaly.

We note that the dense lower crust in Figure 8 has been modeled as a single body with a uniform bulk density contrast with its surroundings. This is not the only explanation of the gravity anomaly. For example, the anomaly could have been modeled equally well with a number of smaller bodies, as has been recently suggested by inversion of magnetotellurics data acquired along the PBAP regional profile [Solon et al., 2016]. These smaller bodies would, however, require higher-density contrasts than the one we have used.

The other main features of the observed Bouguer gravity anomaly are local lows of  $\sim 20$  mGal which we attribute to (1) pre-Silurian narrow graben-like structures, containing sediments of the Jaibaras or Riachão Formations; and/or (2) anorogenic granites equivalent to those that outcrop near the northeast edge of the basin, adjacent to the Jaibaras trough. Unfortunately, the image quality at basement depths along the PBAP reflection profile is poor. However, we note that these anomalies are similar in form to others identified elsewhere in the basin, adjacent to pre-Silurian graben-like structures on shallow focused industry reflection data [e.g., *de Castro et al.*, 2016].

Irrespective of these uncertainties in the origin of the short wavelength gravity anomalies, Figure 8 shows that it is possible to account for the observed Bouguer anomalies in a way that is compatible with the seismic reflection and refraction data. The fact that our best fit model has a relatively dense lower crust is clearly

significant for our understanding of the origin of the basin and key to this is the tectonic subsidence and uplift history of the basin as revealed, for example, by backstripping well and sediment isopach data.

#### 4. Backstripping

We assess the subsidence history of Parnaíba Basin by performing one-dimensional Airy backstripping [e.g., *Watts and Ryan*, 1976; *Steckler and Watts*, 1978; *Sclater and Christie*, 1980] of the sedimentary record from 15 exploration wells that reached crystalline basement or pre-Silurian sediments. The derived curves provide estimates for the depth at which the original crustal surface would have been in the absence of sediment and water loading, thus revealing the subsidence and uplift driven by other tectonic processes.

In order to backstrip, we require the sediment thickness at the time of deposition (i.e., the decompacted sediment thickness) and the paleobathymetry and eustatic sea level changes through time. We decompacted the sediments by assigning grain densities for each formation and calculated the porosity using measurements from well log data. Porosity-depth curves for each well were derived from sonic logs using the *Wyllie et al.* [1956] equation (e.g., Figure 10a). We assumed that porosity loss with depth is purely mechanical (i.e., negligible contribution from other mechanisms such as chemical compaction) and is exponentially decreasing in form, such that best fit exponential functions from our derived porosity-depth curves can be used to simulate decompaction using the depth integrated methods of *Steckler and Watts* [1978] and *Sclater and Christie* [1980].

A notable feature of the Parnaíba porosity-depth curves is that they do not exhibit any detectable “steps” across the Palaeozoic unconformities, implying that away from the basin edges there is not an appreciable amount of sediment that is missing. This is significant, as there is evidence for at least 2 km of Mesozoic inversion along the western margin of the basin [e.g., *Daly et al.*, 2014].

Given that the inferred depositional environments within the basin are predominantly lacustrine and estuarine, shallow marine, and terrestrial (aeolian), we do not include paleobathymetric corrections but instead assign informal errors of  $\pm 100$  m to individual estimates of the tectonic subsidence.

Furthermore, we have examined the effects of eustatic sea level variations by backstripping all of the wells using the Phanerozoic sea level of *Haq and Schutter* [2008]. However, we are uncertain, given its mix of terrestrial and marine lithologies, when, if at all, the Parnaíba Basin was connected to the global ocean and so have not included a sea level correction in the backstripped curves presented here.

Figures 10 and 11 show that backstrip curves from the center of Parnaíba Basin are generally concave up decreasing exponentials, with tectonic subsidence accounting for  $\sim 1200$  m over  $\sim 260$  Myr near the center of the basin. Over 70% of the total tectonic subsidence occurs within the first  $\sim 100$  Myr after basin initiation, at which time the curve kinks slightly with the remaining portion of the subsidence occurring at a much slower rate over the next  $\sim 100$  Myr.

The main departures from a concave up exponential subsidence are in the northern basin (Figure 11), where wells that contain Cretaceous Grajaú Unit (TS-5) sediments, exhibit a marked increase in tectonic subsidence rate during this time. The tectonic subsidence is greatest at the northern edge of the basin, accounting for  $\sim 550$  m over 20 Myr. This subsidence becomes more subdued southward as the unit thins and eventually terminates at  $\sim 6.0^\circ\text{S}$ . It is likely that the opening of the equatorial Atlantic Ocean drove this subsidence, together with the accommodation space that it created.

The concave up exponential character of the cratonic phase of subsidence (i.e., TS-3) suggests a thermal cooling mechanism, similar to that invoked for rift-type basins in extensional settings [e.g., *McKenzie*, 1978; *Steckler and Watts*, 1978; *Cochran*, 1981]. Indeed, *Crosby et al.* [2010] and *Armitage and Allen* [2010] have argued that the tectonic subsidence history of the Congo and Williston cratonic basins can be explained by a rifting model with a stretching factor,  $\beta$ , in the range 1.1–1.3, if the thermal thickness of the lithosphere is of the order of 200 km. The thick lithosphere allows for the prolonged thermal subsidence, as the lithospheric thermal time constant is proportional to the square of the plate thickness.

##### 4.1. Subsidence History Modeling

We have tested the possibility that the tectonic subsidence history derived from backstripping well data in the Parnaíba Basin can be explained by a thermal model in which the crust and mantle lithosphere are thinned at the time of rifting and then subside thermally. We tested a variety of rifting scenarios using the

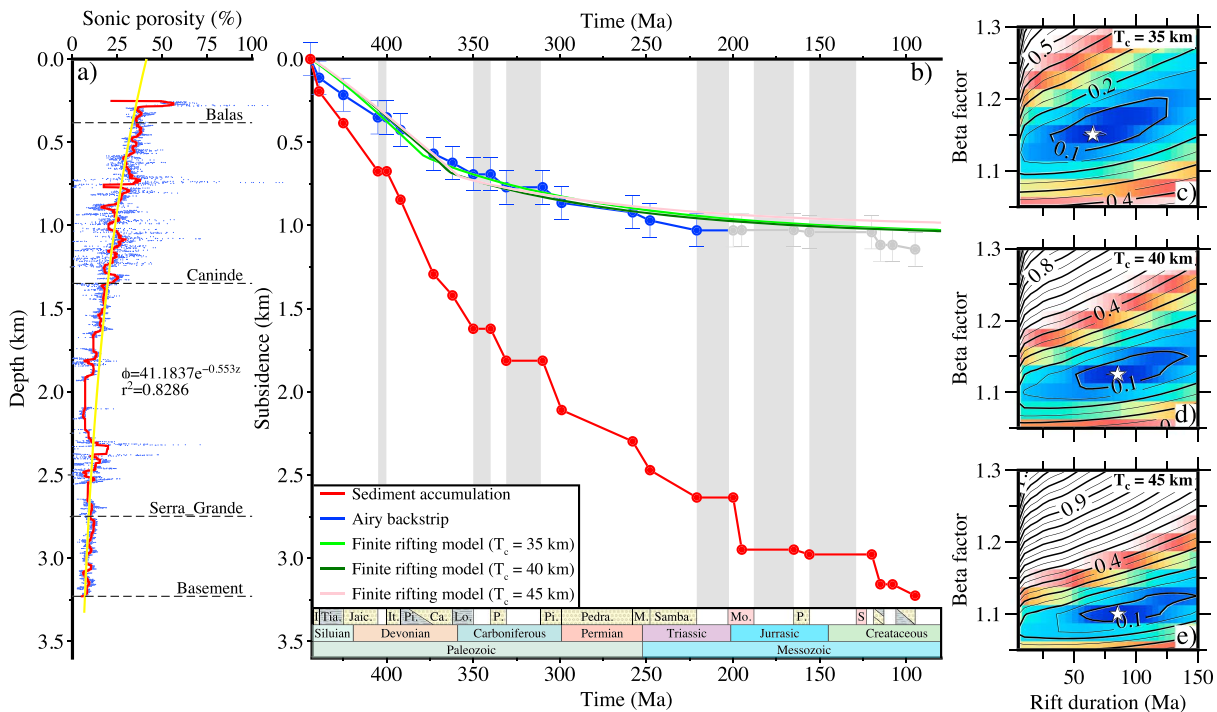


**Figure 10.** Subsidence history at well 2-BAC-001-MA located in the center of Parnaíba Basin. (a) Sonic porosity versus depth. Blue dots are raw data, red line is 100-point median filter, yellow curve is the best fit exponential function, and dashed black lines are megasequence boundaries. (b) Tectonic subsidence and uplift history. Red curve is the total sediment accumulation through time. Blue curve is the backstripped tectonic subsidence once the sediment load is removed and shows the part of the subsidence to which the rifting has been compared. Grey curve shows what we believe to be the postcratonic basin phase of subsidence. Light green, dark green, and pink curves are the best fit model curve based on a finite rifting extension model with a starting crustal thickness of 35, 40, and 45 km respectively. Grey vertical strips show regions of missing section. (c–e) Grid search results for the best fit stretching factor,  $\beta$ , and rift duration assuming a thermal thickness of 170 km for starting crustal thickness of 35, 40, and 45 km.

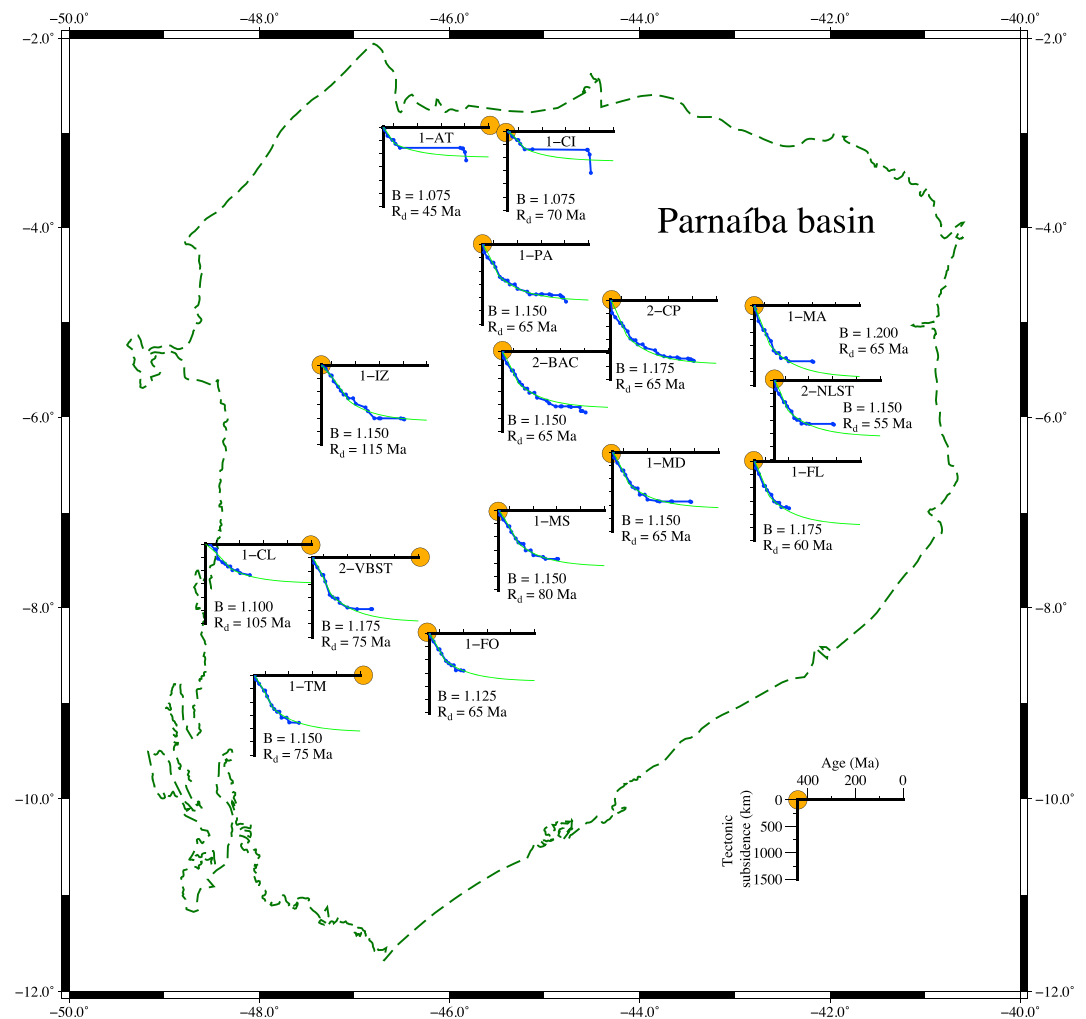
Cochran [1981] modification of the McKenzie [1978] thermal model which includes finite rifting and lateral heat flow and compared the predicted subsidence curves and crustal structures to our observed backstripped curves and Moho depths.

Table 2 summarizes the lithospheric parameters used in our models. We assumed a thermal thickness of the lithosphere of 170 km, similar to that derived using surface wave tomography by Priestley and McKenzie [2013] and that the pre-extended lithosphere had reached this thickness prior to basin initiation.

As discussed by Armitage and Allen [2010], the temperature at the base of the lithosphere would probably have been higher in the Neoproterozoic than at the present day and will have decreased with time, given that the mantle has been cooling at a rate of  $50\text{--}100^\circ\text{C Ga}^{-1}$  [Pollack et al., 1993]. However, similarly to Armitage and Allen [2010], we found that variations in the basal temperature on the order of less than a few hundred degrees had relatively minor effects on the calculated subsidence curves and hence our assumption of a constant basal temperature of  $1333^\circ\text{C}$  is reasonable.

Some authors [e.g., de Castro et al., 2016, 2014; de Oliveira and Mohriak, 2003] have suggested that the Jaibaras Group represents a Cambrian synrift, which infills localized grabens that formed through reactivation of the Neoproterozoic shear zones (TBSZ and subsidiaries). In this scenario, the Phanerozoic cratonic basin sequence reflects a long-lived postrift sequence associated with a widespread (i.e., nonlocalized) rifting event.

We tested this hypothesis by calculating the tectonic subsidence curves for a range of rift durations and  $\beta$  factors for a rifting event beginning at different times during the Early Paleozoic. Figure 11 compares the observed backstrip curves at the 2-BAC-001-MA well to the calculated subsidence assuming an initial rifting age of 444 Ma (i.e., base Silurian). The figure shows that the best fit is for a rift duration of 75 Myr and  $\beta = 1.15$ , assuming a thermal thickness of the lithosphere of 170 km. This parameter pair implies a depth to Moho beneath the well of  $35\text{ km}/1.15 + 3.5\text{ km} = 33.7\text{ km}$  which is significantly less than the minimum Moho depth of 41 km that we have derived from the wide-angle seismic data (Figures 5 and 6).



**Figure 11.** Tectonic subsidence curves for all wells that reach basement or pre-Silurian sediments (location, orange filled circle). Airy backstrip (blue) and modeled (green) subsidence curves. The best fit stretching factor,  $\beta$ , and rift duration ( $R_d$ ) are indicated for each well. Note that best fit curves are only fit the TS3 (cratonic basin) phase of the subsidence history.

We have also tested this model using a thicker initial crustal thickness than 35 km (Figures 10c–10e). An equally good fit to the observed subsidence data can be achieved using a range of initial thicknesses, with an initial crustal thickness of  $\sim 42$  km required in order to reproduce the seismically observed Moho depth. We believe, however, that an initial crustal thickness  $>40$  km is unlikely for two reasons: (1) seismically derived present-day crustal thickness in the flanking regions of the basin is less than or equal to 40 km, typically  $\sim 32$ – $38$  km (Figure 9) [e.g., *Assumpção et al.*, 2013; *Luz et al.*, 2015] and (2) most of the early sediments of Serra Grande megasequence were deposited at or near sea level. This is significant as global compilations of crustal thickness [*Bassin et al.*, 2000] and elevation [*Amante and Eakins*, 2009] show a peak at 30–32 km for elevations of  $\pm 200$  m, while thicknesses of  $>40$  km are usually associated with high topography due to isostasy. Irrespective of whether the depth to Moho can be reproduced, a rifting mechanism is also inconsistent with the regional reflection profile (Figure 3) which lacks extensional strain features, as well as our gravity modeling (sections 3.4 and 4.2) and the morphology of the basin depocenter through space and time, as discussed below.

While Airy backstripping of the sedimentary record from individual wells reveals the tectonic subsidence and uplift history at a single point, flexural backstripping of sediment isopach grids has the potential to reveal the tectonic history of a basin as a function of both space and time.

Figure 12 shows the flexural backstrip for formations from TS-3 to TS-5 megasequences, calculated from regional sediment isopach grids of all the available well data (Figure S12). We assumed a range of elastic

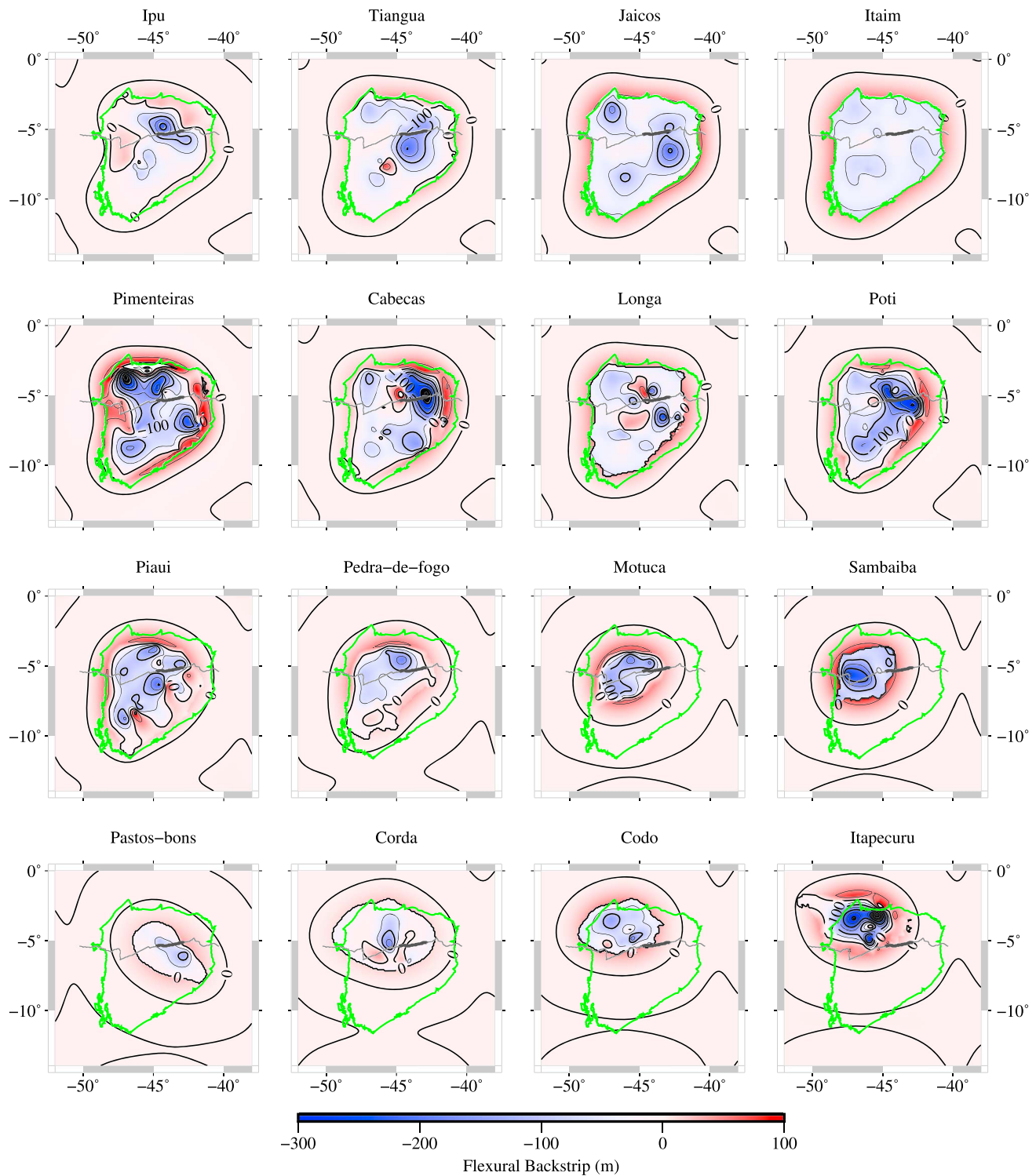


**Figure 12.** Flexural backstripping assuming a constant  $T_e$  of 50 km of the Ipu through Itapecuru Formations of tectonostratigraphic Units 3–5 (Figure 2) showing the change in tectonic subsidence and uplift as a function of space and time. The backstrip shows a bowl-shaped region of subsidence that is flanked by uplifts and persists from the earliest to the latest stages of basin evolution. Green line shows the present-day extent of Parnaíba Basin. Grey line shows the location of the PBAP seismic reflection profile. Thick dark grey line shows the extent of the MCR. The figure shows that the basin depocenter started to shift northwestward during the Pedra-de-Fogo Formation and during TS-5, appears constrained to the northwest and significantly smaller than during the TS-3.

thickness in the backstripping ( $5 < T_e < 75$  km) and found that the general patterns of tectonic subsidence and uplift do not change significantly with elastic thickness. The figure shows that the earliest formation, Ipu, is characterized by a broad region of subsidence that is flanked by uplifts. The maximum subsidence was located in the center (in the region of the MCR), and this basin shape appears to persist through the Pimenteiras and into the Longa Formation. The tectonic subsidence and uplift patterns then change: the basin narrows and by the time of the Sambaiba Formation, the main depocenter along with its flanking bulges appears to have shifted to the west. The shifts are most apparent on the eastern margin of the basin, although we believe that they may also occur on the western margin of the basin, but reactivation during the Mesozoic has obscured them.

The persistence of a broad sag basin from the Ipu through to the Longa Formations is of particular interest because this corresponds in time to when the best fit thermal model to the backstrip data (Figure 10) predicts that rifting is occurring. In rift basins, synrift sequences are normally deposited in localized narrow half grabens, while the overlying postrift sequences form a broad linear regional sag. The figure suggest that the Parnaíba Basin began as a broad sag and has actually decreased in areal extent rather than increased with time, which casts further doubt on the applicability of a rifting model to the basin.

#### 4.2. Process-Oriented Gravity Anomaly Modeling

In order to quantify the role that rifting could have played in the development of the basin, we have used a Process-Oriented Gravity Modeling (POGM) technique [Watts, 1988] in which the sediment thickness is backstripped (either along a profile or as a grid) and the gravity anomalies due to rifting and its associated crustal thinning computed, combined with the gravity effect of sediment loading and its flexural compensation, and compared to observations. POGM has been successfully applied to a number of rift-type basins in the East Coast USA, Mozambique, Antarctica, and India margins [e.g., Watts, 2001; Close *et al.*, 2009; Krishna *et al.*, 2000] where it has been used to constrain the elastic thickness,  $T_e$ , of extended continental lithosphere and the location of the ocean-continent boundary.

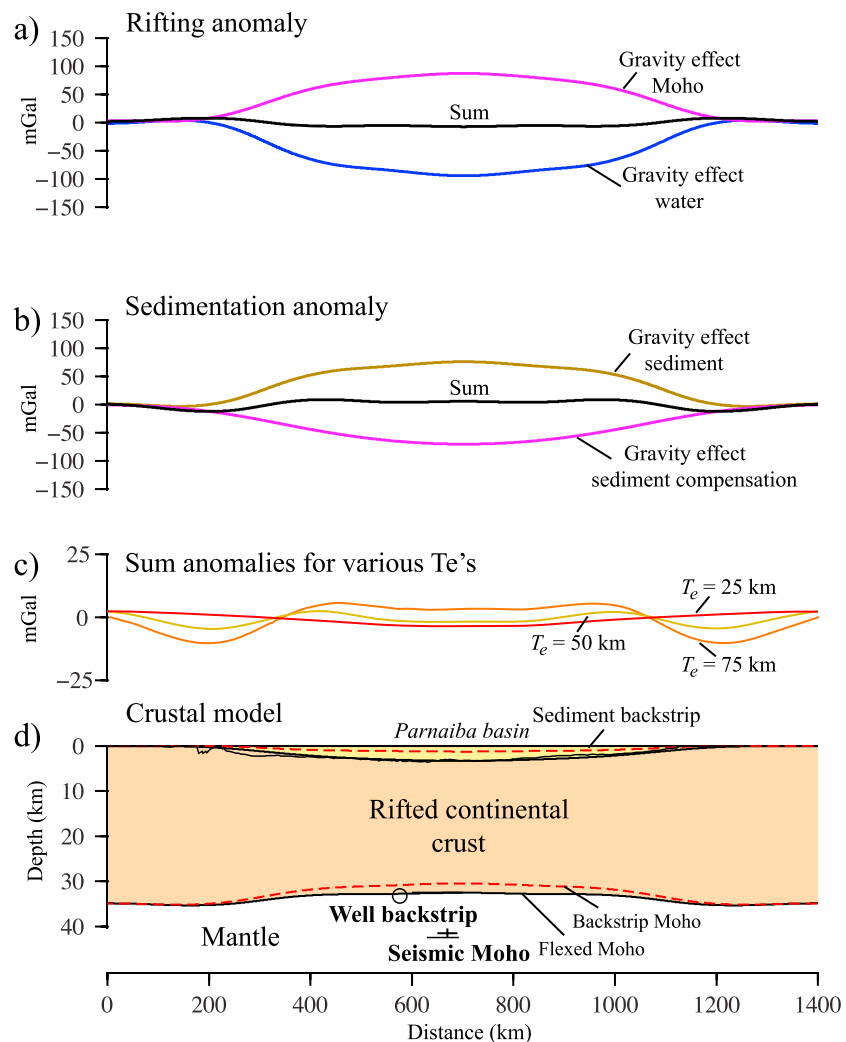
POGM, as described by Watts [2001], is a three-step process. First, the known sediment distribution is flexurally backstripped for a particular  $T_e$  and the backstrip used to restore the crustal structure at the time of rifting assuming isostasy. Second, the “rifting anomaly” is calculated from the sum of the negative gravity effect of the backstripped, water (or air) filled subsidence, and the positive gravity effect of the thinned, rifted crust and the “sedimentation anomaly” is given by the sum of the gravity effect of the sediment load and its flexural compensation. Finally, the rifting anomaly and sedimentation anomaly are summed and compared to the Parnaíba gravity anomaly.

Figure 13 shows the “rifting,” “sedimentation,” and “sum anomaly” for a zero elevation, 1000 km wide, and 3.5 km deep symmetric basin, of similar geometry to Parnaíba Basin. The assumed values of the unstretched, zero elevation crustal thickness and density of water, sediments, crust, and mantle are listed in Table 2. The rifting anomaly shows a subdued edge effect “high to low” couple, typical of rifted margins. The sedimentation anomaly shows a broad high and two flanking lows due to the mass excess of the sediments and the mass deficiency of their flexural compensation. As would be expected for an isostatic process, the sum anomaly averages to zero and comprises a small amplitude high over the basin center, which is flanked by a broad low.

Comparison of the predicted depths to Moho and gravity anomalies to observations shows significant discrepancies. First, the predicted depth to Moho is less than the seismic depth to Moho as predicted by wide-angle seismic data. Second, the predicted anomalies are near zero, in contrast to the observed Bouguer anomaly which exhibits a regional negative anomaly of  $\sim -30$  mGal. Again, we have repeated this calculation for a range of initial crustal thicknesses (Figure S13), which show that the resulting anomaly is very similar for all values within reasonable bounds (25–45 km).

### 5. Discussion

We have shown, from considerations of the depth to Moho, tectonic subsidence, and gravity anomaly, that a rifting model in which the crust is thinned and heated at the time of rifting is unable to explain the observed crustal structure, subsidence history, and Bouguer gravity anomalies of the Parnaíba Basin. Clearly then, other processes must be involved.



**Figure 13.** Process-Oriented Gravity Modeling (POGM) of a symmetric basin with a similar geometry (i.e., width and depth) to the Parnaíba Basin assuming that the only processes that are operative are rifting, which thins the crust, and sediment loading. The rifting and sedimentation anomalies were calculated using a line integral method [Talwani *et al.*, 1959]. The thickness of zero elevation crust and the densities assumed for the water, sediment, crust, and mantle are summarized in Table 2. (a) Gravity effect of rifting showing the individual contributions from the water-filled depression and the elevation of the Moho. (b) Gravity effect of the sediment load and its compensation at the sediment/basement and crust/mantle interfaces. (c) Sum anomalies obtained by summing the rifting and sedimentation anomalies. (d) Crustal model. The modeling shows that irrespective of the elastic thickness, a rifting model predicts near zero gravity anomalies and a shallower Moho beneath the basin than its flanks.

The high-density lower crust inferred from gravity modeling (Figure 8), together with the deeper seismic Moho beneath the basin than flanking regions, suggest that magmatic intrusions, buried loading, and its associated surface flexure might have played some role in providing accommodation space for sediments to infill. Such intrusions have been invoked before in order to explain gravity anomaly data over the Amazon [Nunn and Aires, 1988], Paraná [Mariani *et al.*, 2013], and Williston [DeRito *et al.*, 1983] Basins. Nunn and Aires [1988], for example, have proposed that magmatic intrusions in the lower crust might have caused up to 4 km of the tectonic subsidence in the Middle Amazon cratonic basin, sufficient to cause a basin with >6 km of sediment.

In the Michigan Basin, Haxby *et al.* [1976] proposed that a diapiric rise of hot asthenosphere into the lower crust caused a transformation of the lower crust gabbro into eclogite. As the lower crust cooled, the basin subsided under the load of the eclogite. Baird *et al.* [1995] also inferred eclogization of the lower crust in the Williston basin based on seismological evidence. However, our gravity data appear to rule out eclogite

within the Parnaíba crust, as this would be expected to exhibit a density contrast on the order of  $\sim 400\text{--}500\text{ kg m}^{-3}$  which is too large to account for the observed Bouguer gravity anomaly over the basin (Figure 8). Furthermore, to occur on timescales relevant to basin initiation, the gabbro-garnet granulite-eclogite phase transition requires the presence of interstitial water [Ahrens and Schubert, 1975], and as discussed by Armitage and Allen [2010] this is an unlikely condition in dry cratonic regions, which are isolated from processes that may produce large-scale hydration such as subduction.

In order to examine whether buried loading could account for the gravity data over the Parnaíba Basin, we have used POGM to calculate the gravity effect of buried loading and compared it to observed Bouguer gravity anomalies. First, we used the seismic and gravity data (e.g., Figures 5 and 8) to determine the physical parameters (i.e., width, thickness, and density contrast) of the buried load and then used it to compute the surface and Moho flexure and the resulting gravity anomalies assuming that the surface flexure it causes is infilled by air or water. This is the so-called "buried loading" anomaly. Second, sediments are assumed to infill the surface flexure by displacing either air or water and load the crust causing additional flexure of the basement and Moho. This is the sedimentation anomaly. Finally, the sum is calculated by combining the buried loading and sedimentation anomalies (Figure 14).

Figure 15 compares the sum anomalies from POGM of rifting and buried loading to the observed Bouguer gravity anomaly. For the purposes of the comparison, we have extended the measured gravity anomalies along the PBAP seismic reflection profile by  $\sim 150\text{ km}$  using data sampled from the  $2.5 \times 2.5\text{ min}$  EGM2008 gravity field model. The figure shows that a rifting model is unable to explain the observed gravity Bouguer anomaly. Only a buried loading model in which a dense body in the lower crust causes a surface flexure into which sediments can accumulate appears capable of explaining the gravity data.

We conclude therefore that buried loading, in combination with sediment loading, can explain our observations. In particular, we are able to produce the maximum tectonic subsidence obtained by backstripping well data ( $\sim 1.2\text{ km}$ ) and to approximately match both the long wavelength Bouguer gravity anomaly field and Moho depth constrained using wide-angle reflection data (Figure 5d).

The main outstanding questions are as follows: "Can buried loading explain the subsidence history of the basin?" and, if it can, "Where is the evidence in the basin of its associated magmatism?"

We know from volcano loading [e.g., Watts and Zhong, 2000] that the elastic thickness of oceanic lithosphere,  $T_e$ , is a function of both plate and load age. The strength of the lithosphere increases with plate age as it cools, increases its density, and increases its depth with age, such that old seafloor is more rigid than young seafloor. But strength decreases with load age as the lithosphere relaxes from its short-term thickness to its long-term elastic thickness. There is therefore a "competition" between thermal cooling, which works to strengthen the plate, and a load-induced stress relaxation that weakens it.

Watts and Zhong [2000] used a multilayered viscoelastic model in which the effective viscosity of the lithosphere is determined from its thermal structure to show that volcano loads would be supported initially by a thick, essentially elastic, structure that would then weaken with time. For example, volcano loads emplaced on 80 Ma seafloor would relax rapidly, such that  $\sim 50\%$  of the final subsidence is achieved within the first  $\sim 50,000$  years following load emplacement. The rate of subsidence depends on thermal age: young seafloor subsides more rapidly than old seafloor. As the subsidence increases with age since loading, flanking flexural bulges migrate in toward the load.

Thermal considerations, kimberlite and xenolith nodules, and geochemical calculations suggest significant differences in the viscosity structure between oceanic and continental cratonic lithospheres. Dixon *et al.* [2004], for example, suggest that the viscosity at 75–125 depths in dry cratons is  $10^{23}\text{--}10^{25}\text{ Pa s}$ , assuming a uniform strain rate of  $10^{-15}\text{--}10^{-16}\text{ s}^{-1}$ , which is an order of magnitude greater than at equivalent depths in oceanic lithosphere. A consequence of the viscosity structure is that when cratonic lithosphere is loaded, it would be expected to undergo a stress relaxation over much longer times than would oceanic lithosphere.

Unfortunately, there are no constraints on the thermal and, hence, viscosity structure of the Parnaíba block lithosphere. We have therefore constructed a simple model for the viscosity structure to determine if at least part of the observed subsidence of the Parnaíba Basin could be attributed to a viscoelastic stress relaxation following emplacement of a buried load.

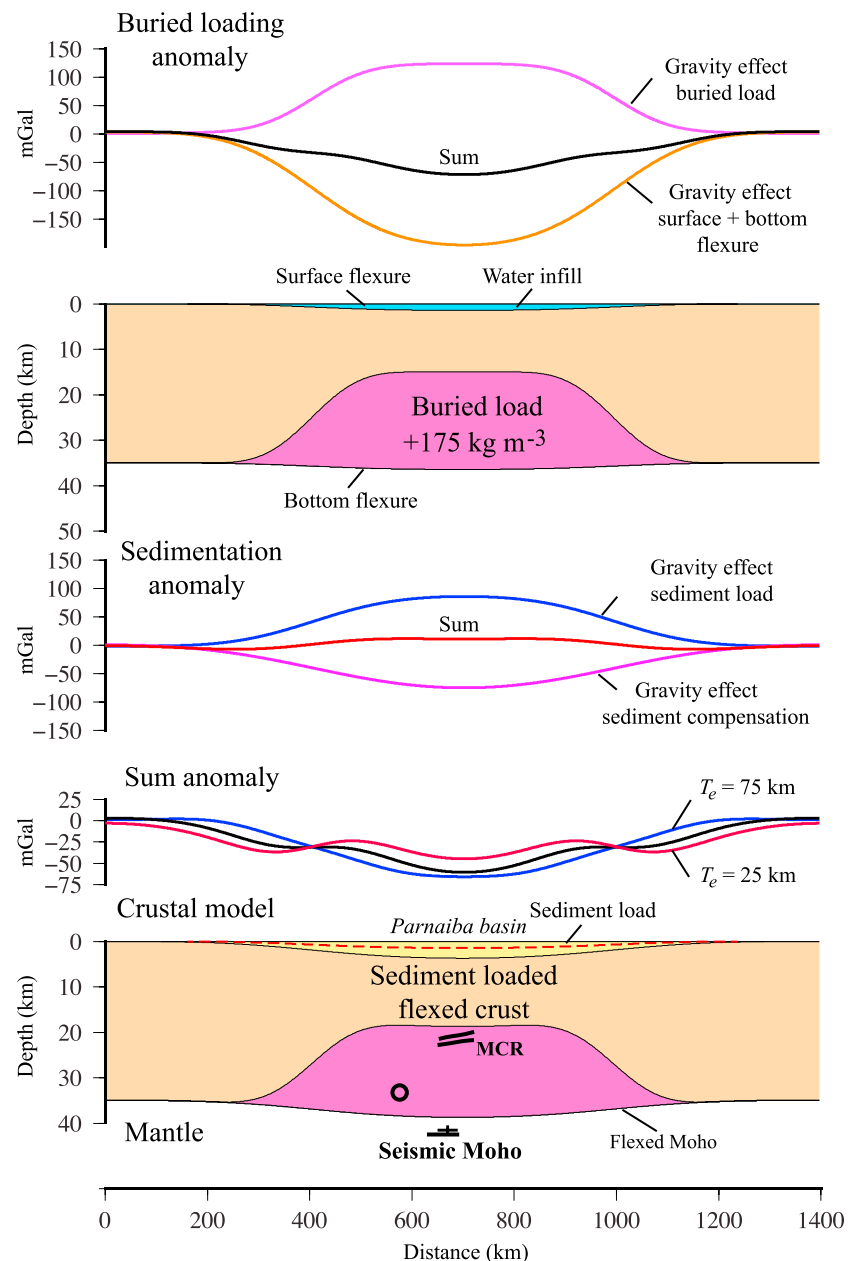


**Figure 14.** Process-Oriented Gravity Modeling (POGM) of a sedimentary basin with a similar geometry (i.e., width and depth) to the Parnaíba Basin that formed by buried loading. The gravity effect of buried loading and its resulting water-filled surface flexure was calculated using the same method densities and  $T_e$  as assumed in Figure 13. (a) Gravity effect of buried loading showing the individual contributions from the buried load and its resulting water-filled surface flexure. (b) Crustal model. (c) Gravity effect of the sediment load and its compensation at the sediment/basement and crust/mantle interfaces. (d) Sum anomalies obtaining by adding the buried and sediment gravity anomalies. (e) Crustal model. The modeling shows that irrespective of the assumed elastic thickness, negative gravity anomalies are predicted. In addition, Moho occurs at a deeper depth beneath the basin than its flanks.

Figure 16 shows the calculated subsidence due to a buried load, the size of which has been constrained by our gravity and seismic data, emplaced on a multilayered viscoelastic plate model. We assumed a simple three-layer model comprising an upper 0–50 km high viscosity, essentially elastic, layer, a middle 50–75 km layer of viscosity  $10^{27}$  Pa s, and a lower 75–300 km layer with a viscosity of  $10^{24}$  Pa s. The viscosity selected for the lower layer is within the range suggested by Dixon *et al.* [2004] for a dry rheology craton. The figure shows a rapid initial subsidence that is followed by a slow exponentially decreasing

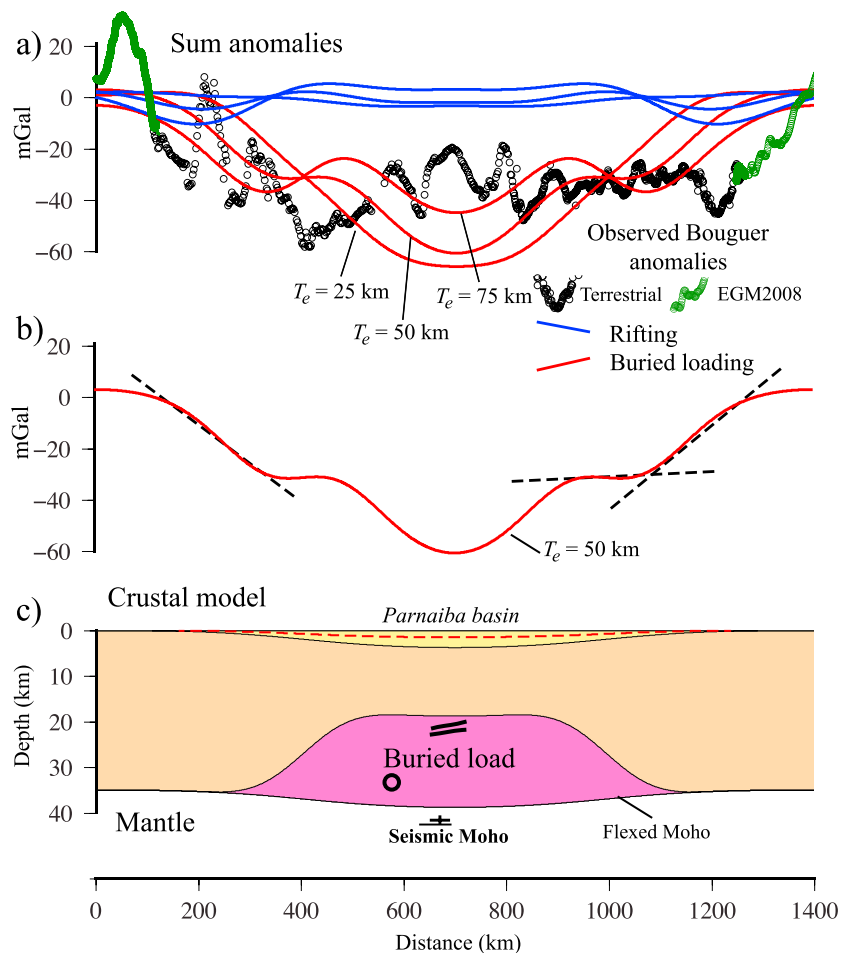


**Figure 15.** Summary diagram showing the results of Process-Oriented Gravity Modeling (POGM). (a) Comparison of the observed Bouguer gravity anomalies (black + green open circles) to the calculated sum anomalies derived from POGM of rifting (blue curves) and buried loading (red curves). (b) Calculated gravity anomaly for buried loading with  $T_e = 50$  km. Dashed black lines show those segments of the calculated gravity anomalies that explain the observed anomalies particularly well. (c) Crustal structure implied by the buried loading model.

subsidence. The pattern of subsidence reflects the fact that the deeper hotter low viscosity layers lose their strength first through thermally activated creep while the shallower colder layers lose their strength much more slowly.

The figure shows that a load induced viscoelastic stress relaxation could indeed contribute to the long tectonic subsidence history as recorded in deep wells in the Parnaíba Basin. In particular, stress relaxation explains the exponential nature of the subsidence, which is recorded in each of the Parnaíba Basin wells. We tested a range of viscosity models and found that they all predict an exponentially decreasing subsidence. However, only models in which the viscosity of the lowest viscosity layer was  $\sim 10^{24}$  Pa s can explain the long-term basin subsidence: higher viscosities produced too slow a subsidence and lower viscosities too rapid a subsidence.

Irrespective of the actual viscosity structure, we found that most models in which the viscosity decreases with depth predict stratigraphic offlap at the edges of the basin. This is because as the lithosphere relaxes, the load-induced subsidence increases, and the flanking bulges migrate in toward the load. Offlap, which is well developed in the Devonian and Carboniferous at the eastern edge of the Parnaíba Basin, will be further enhanced by regional uplift and erosion. However, it will be obscured by structural inversion subsequent to basin initiation, such as may have occurred at the western edge of the basin during the Mesozoic.

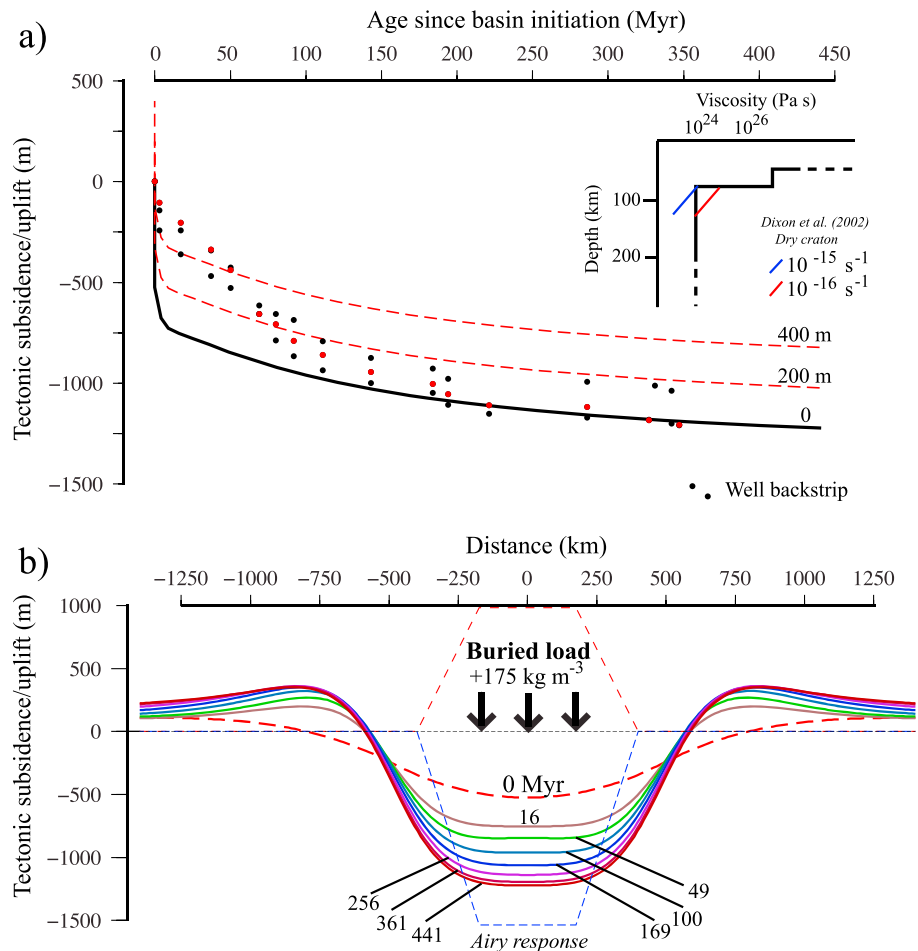


**Figure 16.** Comparison of the observed and calculated subsidence of a multilayered viscoelastic model caused by a buried load. The observed subsidence is based on the tectonic subsidence derived from backstripping wells in Figure 11. Black filled circles show wells that reached basement. Red filled circles show the backstripped tectonic subsidence at the 2-BAC-001-MA well in the center of the basin (Figure 11). The calculated subsidence is based on a buried load with a geometry (i.e., top radius and bottom radius and height) constrained by the seismic and gravity data shown Figure 8 and the viscosity structure shown in the inset. Black line = calculated subsidence. Red dashed lines = subsidence shifted vertically by 200 (lower curve) and 400 m (upper curve). (a) Subsidence as a function of age since basin initiation at 443 Ma (i.e., base Silurian). (b) Subsidence as a function of distance across the (assumed) symmetric buried load.

One difficulty with the buried load model is not knowing precisely its location within the plate. While it seems likely that the upper surface of the buried load is defined by the MCR and the source of the gravity anomaly high is located in the crust, we lack precise constraints, for example, from seismic refraction data, on whether the buried load is confined to the lower crust or whether some or all of the load extends into the upper mantle.

A potentially more difficult problem if the buried load is a magmatic body is why, given its large size, we do not see more evidence of magmatism at the time of basin initiation. Klein and Moura [2008] and Ganade de Araujo et al. [2014a] have described 650–620 Ma old extensive subduction-related calc-alkaline magmatism and precollisional to syncollisional metavolcano-sedimentary sequences, 620–570 Ma old collisional plutonism, 580–510 Ma old post-tectonic, and 500–460 Ma anorogenic plutonism, uplift, and extrusion tectonics from the Borborema Province which flanks Parnaíba in the east. However, the areal extent of the granites is small and occurrences of similar age magmatism in the adjacent São Luís and Amazonia cratons which flank Parnaíba in the north and west, respectively, appears to be limited.

One possibility is that the magmatism is obscured by the Early Paleozoic cover sediments of Parnaíba. Indeed, a high conductivity “block” of magmatic material has been inferred in the basement beneath the center of

the basin using electromagnetic methods [Arora *et al.*, 1999]. Another possibility is that one or more regional erosional events resurfaced the Parnaíba block prior to deposition of the Silurian and so removed much of the evidence for magmatism.

We have, thus far, only considered the mechanical effects of a single buried load that is emplaced in the plate, which then relaxes with time. The plume-like diapiric rise of hot magmatic material in the subcrustal mantle will elevate temperatures and cause uplift and, maybe, erosion, while its intrusion into the lower crust and subsequent cooling and contraction will cause subsidence. For example, Stel *et al.* [1993] have argued that a sill-like intrusion at the Moho will, depending on the amount of erosion, result in a short-term (a few million years) rapid subsidence of the crust due to crystallization and densification followed by a long-term (a few tens of million years) slow subsidence as the intrusion cools. One consequence of this is that the buried load will vary with time, which we have not taken into account in our modeling.

Other nonplume sources of heating have been proposed to explain the subsidence of cratonic basins. For example, Klein and Hsui [1987] have proposed that thermal insulation at the time of supercontinent assembly results in heating, melting and extension. However, it appears most cratonic basins are located on thick, not thin extended crust and lithosphere [Priestley and McKenzie, 2013]. McKenzie and Priestley [2016] have suggested therefore that appreciable crustal thickening during orogeny, internal radiogenic heating, and then rapid erosion of ~40 km of crustal material might account for the long-term subsidence of cratonic basins. Although there is evidence for a Neoproterozoic orogenic belt near the region now occupied by Parnaíba Basin [e.g., Ganade de Araujo *et al.*, 2014b], such a process should result in the emplacement of granulite grade metamorphic rocks at upper crustal levels. This is at odds with basement lithologies encountered in exploration wells within Parnaíba Basin, which include lower grade phyllites and schists. The upper crustal  $V_p$  values (~6.0–6.3 km s<sup>-1</sup>) we derived in the center of the basin (Figure 5d) also appear lower than would be expected from high-grade rocks exhumed from >40 km depth.

We have focused our discussion here on plate processes such as flexure and so have not considered other nonisostatic processes such as those associated with mantle dynamics. As a number of workers have pointed out, upwelling and downwelling asthenospheric flow due, for example, to subducting slabs, may exert tractions on the base of the lithosphere which responds by vertical motions [Burgess and Moresi, 1999; Hager and Richards, 1989]. While the magnitude of such motions is in dispute [Molnar *et al.*, 2015], several workers have proposed dynamic topography as a source for the subsidence and uplift of sedimentary basins, including basins that were previously considered dominated by orogenic loading and flexure [e.g., Liu and Nummedal, 2004]. Downey and Gurnis, [2009] have argued on the basis of its bowl-shape and its close association with a region of high S wave speeds in the subcrustal mantle that the Congo cratonic basin may be a localized region of downwelling in the mantle. Indeed, the ratio of the long wavelength free-air gravity anomaly to topography over the basin (~40 mGal/km) is similar to what would be expected from models of convective downwelling. However, it seems that while dynamic topography might explain some part of the subsidence of cratonic basins on short geological time scales (i.e., tens of million years), for example, the Michigan Basin during the Ordovician [Coakley and Gurnis, 1995], it is difficult to explain how such a mechanism could explain the persistence of cratonic basin subsidence on long time scales (i.e., a few hundreds of million years). We believe therefore that plate processes such as those involved in flexural isostasy are a more likely source of the stresses required to maintain subsidence over the long time scales appropriate for cratonic basin formation.

## 6. Conclusions

1. A 1400 km long seismic reflection profile and split spread seismic reflection and refraction data, together with gravity anomaly and well data, reveal the structure, Phanerozoic evolution and constraints on the origin of Parnaíba cratonic basin.
2. The depth to the pre-Paleozoic basement and Moho beneath the center of the basin is ~3.3 km and ~42.0 ± 2.0 km, respectively. The Moho is as deep or deeper beneath the basin than beneath the Archean and Proterozoic terrains that flank it.
3. The prominent midcrustal reflectivity (MCR) beneath the center of the basin, which can be traced laterally for ~250 km at depths between 17 and 25 km, is underlain by an ~4 s two-way travel time package of continuous to semicontinuous reflectors.

4. Object-oriented gravity modeling suggests that the MCR represents the upper surface of a relatively dense ( $+175 \text{ kg m}^{-3}$ ) body in the lower continental crust, likely to be of magmatic origin.
5. Backstripping of stratigraphic data from wells reveals a concave up, decreasing subsidence, similar to that of rift-type basins. However, beneath the pre-Silurian basin-wide unconformity we see no evidence of extensional strain and Process-Oriented Gravity Modeling suggest that rifting models cannot explain either the observed gravity anomaly or depth to seismic Moho.
6. The best fit to the observed seismic and Bouguer gravity anomaly data is for a model in which the dense body loads the crust and lithosphere, the surface flexural response to which is then infilled by air or water and loaded by sediments.
7. A dense load emplaced in a viscoelastic plate that relaxes on time-scales of several tens of million years is in accord with well data and observations of stratigraphic offlap at the basin edge, although other factors such as thermal cooling, loading history and plate strengthening following magma intrusion may also contribute.

### Acknowledgments

Funding for the seismic data, associated fieldwork, and figure production for this paper have been provided by BP Plc as part of its Parnaíba Basin Analysis Project (PBAP). Seismic and well data were provided by Global Geophysical and the Agência Nacional do Petróleo and gravity data by the Observatório Nacional, Rio de Janeiro. We are grateful to Lucy Andrew (Oxford) for her help in the field, Milton Porsani and Rafael Manenti (Federal University of Bahia) for discussions on the amplitude relief plots presented in Figure 3, Jacob Smith (Oxford) for assistance in data analysis, and John Armitage for helpful comments on an earlier version of the manuscript. Other figures were constructed using Globe Claritas, Fatiando a Terra [Uieda *et al.*, 2013] and GMT [Wessel and Smith, 1991]. Data that support or underlie the conclusions in this paper can be found in the supporting information Figures S1–S13.

### References

- Ahern, J. L., and S. R. Mrkvicka (1984), A mechanical and thermal model for the evolution of the Williston Basin, *Tectonics*, 3, 79–102, doi:10.1029/TC003i001p00079.
- Ahrens, T. J., and G. Schubert (1975), Gabbro-eclogite reaction rate and its geophysical significance, *Rev. Geophys.*, 13(2), 383–400, doi:10.1029/RG013i002p00383.
- Allen, P. A., and J. J. Armitage (2011), Cratonic Basins, in *Tectonics of Sedimentary Basins: Recent Advances*, edited by C. Busby and A. Azor, John Wiley, Ltd, Chichester, U. K., doi:10.1002/9781444347166.ch30.
- Alvarenga, C. J. S., C. A. V. Moura, P. S. S. Gorayeb, and F. A. M. Abreu (2000), Paraguay and Araguaia belts, in *Tectonic Evolution of South America*, edited by U. G. Cordani *et al.*, pp. 183–193, 31st Int. Geol. Congr., Rio de Janeiro, Brazil.
- Amante, C., and B. W. Eakins (2009), ETOPO1 1 arc-minute global relief model: Procedures, data sources and analysis, NOAA Tec. Memo. NESDIS NGDC-24, Natl. Geophys. Data Cent., NOAA, doi:10.7289/V5C8276M.
- Araujo, R. N., A. C. R. Nogueira, J. Bandeira, and R. S. Angelica (2016), Shallow lacustrine system of the Permian Pedra de Fogo Formation, western Gondwana, Parnaíba Basin, Brazil, *J. S. Am. Earth Sci.*, 67, 57–70, doi:10.1016/j.jsames.2016.01.009.
- Armitage, J. J., and P. A. Allen (2010), Cratonic basins and the long-term subsidence history of continental interiors, *J. Geol. Soc. London*, 167, 61–70.
- Arora, B. R., A. L. Padilha, I. Vitorello, N. B. Trivedi, S. L. Fontes, A. Rigoti, and E. H. Chamalaun (1999), 2-D geoelectrical model for the Parnaíba Basin conductivity anomaly of Northeast Brazil and tectonic implications, *Tectonophysics*, 302, 57–69.
- Assumpção, M., M. Bianchi, J. Juliã, F. L. Dias, G. Sand, R. Nascimento, S. Drouet, C. G. Pavão, D. F. Albuquerque, and A. E. V. Lopes (2013), Crustal thickness map of Brazil: Data compilation and main features, *J. S. Am. Earth Sci.*, 43, 74–85.
- Atta-Peters, D., C. A. Achaegakwo, and P. Garrey (2015), Palynofacies, organic geochemical analyses and hydrocarbon potential of the Takorad 11-1 well, Saltpond basin, Ghana, *Pet. Coal*, 57(5), 478–499.
- Baird, D. J., J. H. Knapp, D. N. Steer, L. D. Brown, and K. D. Nelson (1995), Upper-mantle reflectivity beneath the Williston Basin, phase-change Moho, and the origin of intracratonic basins, *Geology*, 23, 431–434.
- Baksi, A. K., and D. A. Archibald (1997), Mesozoic igneous activity in the Maranhao province, northern Brazil:  $^{40}\text{Ar}/^{39}\text{Ar}$  evidence for separate episodes of basaltic magmatism, *Earth Planet. Sci. Lett.*, 15, 139–153.
- Bassin, C., G. Laske, and G. Masters (2000), The current limits of resolution for surface wave tomography in North America, *Eos Trans. AGU*, 81, F897.
- Bellahsen, N., J. M. Daniel, L. Bollinger, and E. Burov (2003), Influence of viscous layers on the growth of normal faults: Insights from experimental and numerical models, *J. Struct. Geol.*, 25(9), 1471–1485, doi:10.1016/S0191-8141(02)00185-2.
- Bizzi, L. A., C. Schobbenhaus, R. M. Vidotti, and J. H. Gonçalves (2003), *Geologia, Tectônica e Recursos Minerais do Brasil*, edited by CPRM, pp. 630–642, UnB, Brasília.
- Blakely, R. J. (1995), *Potential Theory in Gravity and Magnetic Applications*, chap. 9, pp. 182–213, Cambridge Univ. Press, New York.
- Brocher, T. M. (2005), Empirical relations between elastic wavespeeds and density in the Earth's crust, *Bull. Seismol. Soc. Am.*, 95(6), 2081–2092, doi:10.1785/0120050077.
- Burgess, P. M., and L. N. Moresi (1999), Modelling rates and distribution of subsidence due to dynamic topography over subducting slabs: Is it possible to identify dynamic topography from ancient strata?, *Basin Res.*, 11, 305–314.
- Cacace, M., and M. Scheck-Wenderoth (2016), Why intracontinental basins subside longer: 3-D feedback effects of lithospheric cooling and sedimentation on the flexural strength of the lithosphere, *J. Geophys. Res. Solid Earth*, 121, 3742–3761, doi:10.1002/2015JB012682.
- Cannon, J., E. Lau, and R. D. Müller (2014), Plate tectonic raster reconstruction in GPlates, *Solid Earth*, 5, 741–755, doi:10.5194/se-5-741-2014.
- Cella, F. (2015), GTeC-A versatile MATLAB tool for a detailed computation of the terrain correction and Bouguer gravity anomalies, *Comput. Geosci.*, 84, 72–85, doi:10.1016/j.cageo.2015.07.015.
- Christensen, N., and W. D. Mooney (1995), Seismic velocity structure and composition of the continental crust: A global view, *J. Geophys. Res.*, 100(B6), 9761, doi:10.1029/95JB00259.
- Cloetingh, S. (1988), Intraplate stresses: A new element in basin analysis, in *New Perspectives in Basin Analysis*, edited by K. Kleinspehn and C. Paola, pp. 205–230, Springer, New York.
- Close, D. I., A. B. Watts, and H. M. J. Stagg (2009), A marine geophysical study of the Wilkes land rifted continental margin, Antarctica, *Geophys. J. Int.*, 177, 430–450.
- Coakley, B., and M. Gurnis (1995), Far-field tilting of Laurentia during the Ordovician and constraints on the evolution of a slab under an ancient continent, *J. Geophys. Res.*, 100, 613–6327, doi:10.1029/94JB02916.
- Cochran, J. R. (1981), Simple models of diffuse extension and the pre-seafloor spreading development of the continental margin of the northwestern Gulf of Alden, in *Proceedings of the 26th International Congress Symposium on Continental Margins*, *Oceanol. Acta*, pp. 154–165, Geol. of Cont. Margins Symp., Paris.

- Cook, F. (2002), Fine structure of the continental reflection Moho, *Geol. Soc. Am. Bull.*, *114*, 64–79, doi:10.1130/0016-7606(2002)114.
- Cordani, U. G. (1984), Estudo preliminar de integração do Pré-Cambriano com os eventos tectônicos das bacias sedimentares Brasileiras, 15.
- Cordani, U. G., W. Teixeira, M. S. D'Agrella-Filho, and R. I. Trindade (2009), The position of the Amazonian craton in supercontinents, *Gondwana Res.*, *15*, 396–407, doi:10.1016/j.gr.2008.12.005.
- Companhia de Pesquisa de Recursos Minerais (CPRM) (2016), Serviço Geológico do Brasil. Web application. [Available at [http://siagasweb.cprm.gov.br/layout/visualizar\\_mapa.php](http://siagasweb.cprm.gov.br/layout/visualizar_mapa.php).]
- Crosby, A. G., S. Fishwick, and N. White (2010), Structure and evolution of the intracratonic Congo Basin, *Geochem., Geophys., Geosyst.*, *11*, Q06010, doi:10.1029/2009GC003014.
- Daly, M. C., V. Andrade, C. A. Barousse, R. Costa, K. McDowell, N. Piggott, and A. J. Poole (2014), Brasiliano crustal structure and the tectonic setting of the Parnaíba Basin of NE Brazil: Results of a deep seismic reflection profile, *Tectonics*, *33*, 2102–2120, doi:10.1002/2014TC003632.
- de Brito Neves, B. B., R. A. Fuck, U. G. Cordani, and F. A. Thomaz (1984), Influence of basement structures on the evolution of the major sedimentary basins of Brazil: A case of tectonic heritage, *J. Geodyn.*, *1*, 495–510, doi:10.1016/0264-3707(84)90021-8.
- de Castro, D. L., R. A. Fuck, J. D. Phillips, R. M. Vidotti, F. H. R. Bezerra, and E. L. Dantas (2014), Crustal structure beneath the Paleozoic Parnaíba Basin revealed by airborne gravity and magnetic data, Brazil, *Tectonophysics*, *614*, 128–145.
- de Castro, D. L., F. H. Bezerra, R. A. Fuck, and R. M. Vidotti (2016), Geophysical evidence of pre-sag rifting and post-rifting fault reactivation in the Parnaíba Basin, Brazil, *Solid Earth*, *7*, 529–548.
- de Lima, M. V. A. G., J. Berrocal, J. E. P. Soares, and R. A. Fuck (2015), Deep seismic refraction experiment in northeast Brazil: New constraints for Borborema province evolution, *J. S. Am. Earth Sci.*, *58*, 335–349, doi:10.1016/j.jsames.2014.10.007.
- de Matos, R. M. D. (1992), The Northeast Brazilian rift system, *Tectonics*, *11*, 766–791, doi:10.1029/91TC03092.
- de Oliveira, D. C., and W. U. Mohriak (2003), Jaibaras trough: An important element in the early tectonic evolution of the Parnaíba interior sag basin, Northern Brazil, *Mar. Pet. Geol.*, *20*, 351–383.
- de Sousa, M. A. (1996), Regional gravity modelling and geohistory of the Parnaíba Basin (N.E. Brazil), PhD thesis, 107 pp., Univ. of Newcastle, Newcastle upon Tyne.
- DeRito, R. F., F. A. Cozzarelli, and D. S. Hodge (1983), Mechanism of subsidence of ancient cratonic rift basins, *Tectonophysics*, *94*, 141–168.
- Dixon, J. E., T. H. Dixon, D. R. Bell, and R. Malservici (2004), Lateral variation in upper mantle viscosity: Role of water, *Earth Planet. Sci. Lett.*, *222*, 451–467.
- Downey, N. J., and M. Gurnis (2009), Instantaneous dynamics of the cratonic Congo basin, *J. Geophys. Res.*, *114*, B06401, doi:10.1029/2008JB006066.
- Farr, T. G., et al. (2007), The Shuttle radar topography mission, *Rev. Geophys.*, *45*, RG2004, doi:10.1029/2005RG000183.
- Fetter, A. H., W. R. Van Schmus, T. J. S. Santos, J. A. Nogueira Neto, and M. H. Arthaud (2000), U-Pb and Sm-Nd geochronological constraints on the crustal evolution and basement architecture of Ceará State, NW Borborema Province, NE Brazil: Implications for the existence of the Paleoproterozoic supercontinent “Atlantica”, *Rev. Bras. Geociênc.*, *30*, 102–106.
- Fonseca, M. A., C. G. de Oliveira, and H. J. Evangelista (2004), The Araguaia Belt, Brazil: Part of a Neoproterozoic continental-scale strike-slip fault system, *J. Virtual Explor.*, *17*, doi:10.3809/jvirtex.2004.00107.
- Fowler, C. M. R., and E. G. Nisbet (1985), The subsidence of the Williston Basin, *Can. J. Earth Sci.*, *22*, 408–415.
- Ganade de Araujo, C. E., R. F. Weinberg, and U. G. Cordani (2014a), Extruding the Borborema Province (NE-Brazil): a two-stage Neoproterozoic collision process, *Terra Nova*, *26*(2), 157–168, doi:10.1111/ter.12084.
- Ganade de Araujo, C. E., D. Rubatto, J. Hermann, U. G. Cordani, R. Caby, and M. A. S. Basei (2014b), Ediacaran 2,500-km-long synchronous deep continental subduction in the West Gondwana Orogen, *Nat. Commun.*, *5*(October 2015), 5198, doi:10.1038/ncomms6198.
- Góes, A. M. O., and F. J. Feijó (1994), Bacia do Paranaíba, *Bol. Geociênc. Petrobras*, *8*, 57–67.
- Góes, A. M. O., W. A. S. Travassos, and K. C. Nunes (1993), Projeto Parnaíba: Reavaliacao e perspectivas exploratorias, paper presented at Relatorio Petrobras, DEXNOR-DINTER.
- Hager, B. H., and M. A. Richards (1989), Long-wavelength variations in Earth's geoid: Physical models and dynamical implications, *Philos. Trans. R. Soc.*, *328*, 309–327.
- Hamdani, Y., J.-C. Mareschal, and J. Arkani-Hamed (1991), Phase changes and thermal subsidence in intracontinental sedimentary basins, *Geophys. J. Int.*, *106*, 657–665.
- Hamdani, Y., J.-C. Mareschal, and J. Arkani-Hamed (1994), Phase change and thermal subsidence of the Williston Basin, *Geophys. J. Int.*, *116*, 585–597, doi:10.1111/j.1365-246X.1994.tb03282.x.
- Haq, B. U., and S. R. Schutter (2008), A chronology of Paleozoic sea-level changes, *Science*, *322*, 64–68.
- Hartley, R. W., and P. A. Allen (1994), Interior cratonic basins of Africa: Relation to continental break-up and role of mantle convection, *Basin Res.*, *6*(2–3), 95–113, doi:10.1111/j.1365-2117.1994.tb00078.x.
- Haxby, W. F., D. L. Turcotte, and J. M. Bird (1976), Thermal and mechanical evolution of the Michigan Basin, *Tectonophysics*, *36*, 57–75.
- Holt, P. J., M. B. Allen, and J. van Hunen (2015), Basin formation by thermal subsidence of accretionary orogens, *Tectonophysics*, *639*, 132–143, doi:10.1016/j.tecto.2014.11.021.
- Holt, P. J., M. B. Allen, J. van Hunen, and H. M. Bjørnseth (2010), Lithospheric cooling and thickening as a basin forming mechanism, *Tectonophysics*, *495*, 184–194, doi:10.1016/j.tecto.2010.09.014.
- Holzman, M. (1963), Chebyshev optimized geophone arrays, *Geophysics*, *28*, 145–155.
- Howell, P. D., and B. A. van der Pluijm (1999), Structural sequences and styles of subsidence in the Michigan Basin, *Geol. Soc. Am. Bull.*, *111*, 974–991, doi:10.1130/0016-7606.
- Kadima Kabongo, É., S. S. M. Ntabwoba, and F. Lucazeau (2011), A Proterozoic-rift origin for the structure and the evolution of the cratonic Congo Basin, *Earth Planet. Sci. Lett.*, *304*, 240–250, doi:10.1016/j.epsl.2011.01.037.
- Klein, E. L., and C. A. V. Moura (2008), São Luís craton and Gurupi Belt (Brazil): Possible links with the West African craton and surrounding pan-African belts, in *West Gondwana: Pre-Cenozoic Correlations across the South Atlantic Region*, edited by R. J. Pankhurst et al., pp. 137–151, The Geol. Soc., London.
- Klein, G. D. V. (1991), Origin and evolution of North American cratonic basins, *S. Afr. J. Geol.*, *94*, 3–18.
- Klein, G. D. V. (1995), Intracratonic basins, *Tecton. Sediment. Basins*, 459–478.
- Klein, G. D. V., and A. T. Hsui (1987), Origin of cratonic basins, *Geology*, *15*, 1094–1098, doi:10.1130/0091-7613.
- Koptev, A. I., and A. V. Ershov (2011), Quantitative model of thermal thickness of the Earth's lithosphere, in *Materials of the International Conference Devoted to Memory of V.E.Khain “Current State of Sciences About the Earth”*, pp. 924–929, Lomonosov Moscow State Univ., Moscow, 1–4 Feb.
- Krishna, M. R., S. Chand, and C. Subrahmanyam (2000), Gravity anomalies, sediment loading and lithospheric flexure associated with the Krishna-Godavari Basin, eastern continental margin of India, *Earth Planet. Sci. Lett.*, *175*, 223–232.

- Lambeck, K. (1983a), The role of compressive forces in intracratonic basin formation and mid-plate orogenies, *Geophys. Res. Lett.*, *10*, 845–848.
- Lambeck, K. (1983b), Structure and evolution of the intra-cratonic basins of central Australia, *Geophys. J. R. Astron. Soc.*, *74*, 843–886.
- Liu, S.-F., and D. Nummedal (2004), Late Cretaceous subsidence in Wyoming: Quantifying the dynamic component, *Geology*, *32*, 397–400.
- Loureiro, A., A. Afilhado, L. Matias, M. Moulin, and D. Aslanian (2016), Monte Carlo approach to assess the uncertainty of wide-angle layered models: Application to the Santos Basin, Brazil, *Tectonophysics*, *683*, 286–307, doi:10.1016/j.tecto.2016.05.040.
- Ludwig, W. J., J. E. Nafe, and C. L. Drake (1970), Seismic refraction, in *The Sea*, vol. 4, edited by A. E. Maxwell, pp. 53–84, Wiley-Interscience, New York.
- Lucazeau, F., J. Armitage, and E. K. Kabongo (2015), Thermal regime and evolution of the Congo basin as an intracratonic basin, in *Geology and Resource Potential of the Congo Basin*, edited by M. J. de Wit, F. Guillocheau, and M. C. J. de Wit, pp. 229–244, Springer, New York.
- Luz, R. M. N., J. Julià, and A. F. Do Nascimento (2015), Crustal structure of the eastern Borborema Province, NE Brazil, from the joint inversion of receiver functions and surface wave dispersion: Implications for plateau uplift, *J. Geophys. Res. Solid Earth*, *120*, 3848–3869, doi:10.1002/2015JB011872.
- Mariani, P., C. Braitenberg, and N. Ussami (2013), Explaining the thick crust in Paraná basin, Brazil, with satellite GOCE gravity observations, *J. S. Am. Earth Sci.*, *45*, 209–223, doi:10.1016/j.jsames.2013.03.008.
- Mazzarini, F., G. Corti, P. Manetti, and F. Innocenti (2004), Strain rate and bimodal volcanism in the continental rift: Debre Zeyt volcanic field, northern MER, Ethiopia, *J. Afr. Earth. Sci.*, *39*(3–5), 415–420, doi:10.1016/j.jafrearsci.2004.07.025.
- McKenzie, D. P. (1978), Some remarks on the development of sedimentary basins, *Earth Planet. Sci. Lett.*, *40*, 25–32.
- McKenzie, D., and K. Priestley (2016), Speculations on the formation of cratons and cratonic basins, *Earth Planet. Sci. Lett.*, *435*, 94–104, doi:10.1016/j.epsl.2015.12.010.
- Merle, R., A. Marzoli, H. Bertrand, L. Reisberg, C. Verati, C. Zimmermann, M. Chiaradia, G. Bellieni, and M. Ernesto (2011),  $^{40}\text{Ar}/^{39}\text{Ar}$  ages and Sr-Nd-Pb-Os geochemistry of CAMP tholeiites from western Maranhão basin (NE Brazil), *Lithos*, *122*, 137–151, doi:10.1016/j.lithos.2010.12.010.
- Mesner, J. C., and L. C. P. Wooldridge (1964), Maranhao Paleozoic basin and Cretaceous coastal basins, North Brazil, *Bull. Am. Assoc. Pet. Geol.*, *48*, 1475–1512.
- Middleton, M. (1989), A model for the formation of intracratonic sag basins, *Geophys. J. Int.*, *99*, 665–676.
- Milani, E. J., and P. V. Zalan (1999), An outline of the geology and petroleum systems of the Paleozoic interior basins of South America, *Episodes*, *22*, 199–205.
- Milkereit, B., and C. Spencer (1989), Noise suppression and coherency enhancement of seismic data, *Stat. Appl. Earth Sci.*, *89*, 243–248.
- Molnar, P., P. C. England, and C. H. Jones (2015), Mantle dynamics, isostasy, and the support of high terrain, *J. Geophys. Res. Solid Earth*, *120*, 1932–1957, doi:10.1002/2014JB011724.
- Morel-à-l'Huissi, P., A. G. Green, and C. J. Pike (1987), Crustal refraction surveys across the Trans-Hudson Orogen/Williston Basin of south central Canada, *J. Geophys. Res.*, *92*, 6402–6420, doi:10.1029/JB092iB07p06403.
- Moulin, M., D. Aslanian, and P. Unternehr (2010), A new starting point for the South and equatorial Atlantic Ocean, *Earth Sci. Rev.*, *98*, 1–37.
- Moura, C. A. V., B. L. S. Pinheiro, A. C. R. Nogueira, P. S. S. Gorayeb, and M. A. Galarza (2008), Sedimentary provenance and palaeoenvironment of the Baixo Araguaia Supergroup: Constraints on the palaeogeographical evolution of the Araguaia Belt and assembly of West Gondwana, in *West Gondwana: Pre-Cenozoic Correlations Across the South Atlantic Region*, edited by R. J. Pankhurst et al., *Geol. Soc. London Spec. Publ.*, *294*, 297–318, doi:10.1144/SP294.16.
- Naimark, B. M., and A. T. Ismail-Zadeh (1995), Numerical models of a subsidence mechanism in intracratonic basins: Application to North American basins, *Geophys. J. Int.*, *123*, 149–160, doi:10.1111/j.1365-246X.1995.tb06667.x.
- Nunn, J. A., and J. R. Aires (1988), Gravity anomalies and flexure of the lithosphere at the middle Amazon Basin, Brazil, *J. Geophys. Res.*, *93*, 415–428, doi:10.1029/JB093iB01p00415.
- Nunn, J. A., and N. H. Sleep (1984), Thermal contraction and flexure of intracratonic basins: A three-dimensional study of the Michigan Basin, *Geophys. J. R. Astron. Soc.*, *76*, 587–635.
- Pap, A. (1983), Source and receiver arrays, Report compiled for Amoco Research, 208 pp., Canada.
- Pavlis, N. K., S. A. Holmes, S. C. Kenyon, and J. K. Factor (2012), The development and evaluation of the Earth gravitational model 2008 (EGM2008), *J. Geophys. Res.*, *117*, B04406, doi:10.1029/2011JB008916.
- Pollack, H. N., S. J. Hurter, and J. R. Johnson (1993), Heat flow from the Earth's interior: Analysis of the global data set, *Rev. Geophys.*, *31*, 267–280, doi:10.1029/93RG01249.
- Porto, A. L., M. C. Daly, and S. L. Fontes (2016), The pre-Silurian Riachao basin, a new perspective into basement configuration of the cratonic Parnaíba Basin, NE Brazil, paper presented at 48th Congresso Brasileiro de Geologia, Sociedade Brasileira de Geologia, Porto Alegre.
- Priestley, K., and D. McKenzie (2013), The relationship between shear wave velocity, temperature, attenuation and viscosity in the shallow part of the mantle, *Earth Planet. Sci. Lett.*, *381*, 78–91.
- Regone, C. J. (1997), Measurement and identification of 3-D coherent noise generated from irregular surface carbonates, in *Carbonate Seismology*, edited by I. Palaz and K. J. Marfurt, pp. 281–306, Soc. of Explor. Geophys., Tulsa, Okla, doi:10.1190/1.9781560802099.ch11.
- Rossetti, D. F., J. D. S. Paz, and A. M. Góes (2004), Facies analysis of the Codó formation (late Aptian) in the Grajaú area, southern São Luís-Grajaú Basin, *An. Acad. Bras. Cienc.*, *76*, 791–806, doi:10.1590/S0001-37652004000400012.
- Sclater, J. G., and P. A. F. Christie (1980), Continental stretching: An explanation of the post-mid-Cretaceous subsidence of the central North Sea basin, *J. Geophys. Res.*, *85*, 3711–3739, doi:10.1029/JB085iB07p03711.
- Shen, W., R. H. Ritzoller, and V. Schulte-Pelkum (2013), Crustal and uppermost mantle structure in the central U.S. encompassing the midcontinent rift, *J. Geophys. Res. Solid Earth*, *118*, 4325–4344, doi:10.1002/jgrb.50321.
- Sheriff, R. E., and L. P. Geldart (1995), *Exploration Seismology*, chap. 8, pp. 239–348, Cambridge Univ. Press, Cambridge, U. K.
- Sleep, N., J. A. Nunn, and L. Chou (1980), Platform basins, *Annu. Rev. Earth Planet. Sci.*, *8*, 17–34.
- Sleep, N. H. (1971), Thermal effects of the formation of Atlantic continental margins by continental breakup, *Geophys. J. R. Astron. Soc.*, *24*, 325–350.
- Sleep, N. H. (1976), Platform subsidence mechanisms and “eustatic” sea-level changes, *Tectonophysics*, *36*, 45–56, doi:10.1016/0040-1951(76)90005-6.
- Sleep, N. H. (2009), Stagnant lid convection and the thermal subsidence of sedimentary basins with reference to Michigan, *Geochem., Geophys., Geosyst.*, *10*, Q12015, doi:10.1029/2009GC002881.
- Sloss, L. (1963), Sequences in the cratonic interior of North America, *Geol. Soc. Am. Bull.*, *74*, 93–113.
- Sloss, L. (1988), Tectonic evolution of the craton in Phanerozoic time, in *Sedimentary Cover-North American Craton: U.S.*, edited by L. L. Sloss, pp. 25–51, Geol. Soc. of Am., Boulder, Colo.

- Solon, F. F., S. L. Fontes, and E. F. La Terra (2016), Electromagnetic studies in the Parnaíba Basin: Structural characterisation by MT imaging, in *48th Congresso Brasileiro de Geologia*, Porto Alegre.
- Steckler, M. S., and A. B. Watts (1978), Subsidence of the Atlantic-type continental margin off New York, *Earth Planet. Sci. Lett.*, *41*, 1–13.
- Stel, H., S. Cloetingh, M. Heeremans, and P. van der Beek (1993), Anorogenic granites, magmatic underplating and the origin of intracratonic basins in a non-extensional setting, *Tectonophysics*, *226*, 285–299.
- Stern, T. A., W. R. Stratford, A. Seward, C. M. Henderson, M. Savage, E. G. C. Smith, A. Benson, S. Greve, and M. L. Salmon (2010), Crust-mantle structure of the central North Island, New Zealand, based on seismological observations, *J. Volcanol. Geotherm. Res.*, *190*, 58–74.
- Taner, M. T., and Sheriff, R. E. (1977), Application of amplitude, frequency, and other attributes to stratigraphic and hydrocarbon determination, in *Seismic Stratigraphy - Applications to Hydrocarbon Exploration*, AAPG Mem., vol. 26, edited by C. E. Payton, pp. 301–327, Ame. Assoc. of Petrol. Geol., Tulsa, Okla.
- Talwani, M., J. L. Worzel, and M. Landisman (1959), Rapid gravity computations for two-dimensional bodies with application to the Mendocino submarine fracture zone, *J. Geophys. Res.*, *64*, 49–59, doi:10.1029/JZ064i001p00049.
- Trindade, V. S. F., M. D. A. Carvalho, and L. Borghi (2015), Palynofacies patterns of the Devonian of the Parnaíba Basin, Brazil: Paleoenvironmental implications, *J. S. Am. Earth Sci.*, *62*, 164–175, doi:10.1016/j.jsames.2015.06.001.
- Uieda, L., V. C. Oliveira Jr., and V. C. F. Barbosa (2013), Modeling the Earth with Fatiando a Terra, paper presented at Proceedings of the 12th Python in Science Conference.
- Ussami, N., and E. C. Molina (1999), Flexural modeling of the Neoproterozoic Araguaia belt, central Brazil, *J. S. Am. Earth Sci.*, *12*, 87–98.
- Vacher, P., and A. Souriau (2001), A three-dimensional model of the Pyrenean deep structure based on gravity modelling, seismic images and petrological constraints, *Geophys. J. Int.*, *145*(2), 460–470, doi:10.1046/j.0956-540x.2001.01393.x.
- Van Der Voo, R., and D. R. Watts (1978), Paleomagnetic results from igneous and sedimentary rocks from the Michigan Basin, *J. Geophys. Res.*, *83*, 5844–5848, doi:10.1029/JB083iB12p05844.
- Vaz, P. T., N. G. A. M. Rezende, J. R. Wanderley Filho, and W. A. S. Travassos (2007), Bacia do Parnaíba. Boletim de Geociências da Petrobrás, *Rio de Janeiro*, *15*(2), 253–263.
- Watts, A. B. (1988), Gravity anomalies, crustal structure and flexure of the lithosphere at the Baltimore canyon trough, *Earth Planet. Sci. Lett.*, *89*, 221–238.
- Watts, A. B. (2001), Gravity anomalies, flexure and crustal structure at the Mozambique rifted margin, *Mar. Pet. Geol.*, *18*, 445–455.
- Watts, A. B., and W. B. F. Ryan (1976), Flexure of the lithosphere and continental margin basins, *Tectonophysics*, *36*, 25–44.
- Watts, A. B., and S. Zhong (2000), Observations of flexure and the rheology of oceanic lithosphere, *Geophys. J. Int.*, *142*, 855–875.
- Wessel, P., and W. H. F. Smith (1991), Free software helps map and display data, *Eos. Trans. AGU*, *72*, 441–446.
- Wyllie, M. R. J., A. R. Gregory, and L. W. Gardner (1956), Elastic wave velocities in heterogeneous and porous media, *Geophysics*, *21*, 41–70, doi:10.1190/1.1438217.
- Xie, X., and P. L. Heller (2009), Plate tectonics and basins subsidence history, *Geol. Soc. Am. Bull.*, *121*, 55–64.
- Zelt, C. A. (1999), Modelling strategies and model assessment for wide-angle seismic traveltimes data, *Geophys. J. Int.*, *139*, 183–204.
- Zelt, C. A., and R. B. Smith (1992), Seismic traveltimes inversion for 2-D crustal velocity structure, *Geophys. J. Int.*, *108*, 16–34.
- Zhu, T., and L. D. Brown (1986), Consortium for continental reflection profiling michigan surveys reprocessing and results, *J. Geophys. Res.*, *91*, 11,477–411,495, doi:10.1029/JB091iB11p11477.